

## **General Disclaimer**

### **One or more of the Following Statements may affect this Document**

- This document has been reproduced from the best copy furnished by the organizational source. It is being released in the interest of making available as much information as possible.
- This document may contain data, which exceeds the sheet parameters. It was furnished in this condition by the organizational source and is the best copy available.
- This document may contain tone-on-tone or color graphs, charts and/or pictures, which have been reproduced in black and white.
- This document is paginated as submitted by the original source.
- Portions of this document are not fully legible due to the historical nature of some of the material. However, it is the best reproduction available from the original submission.

(NASA-CR-148540) THE INTERACTION OF  
UNIDIRECTIONAL WINDS WITH AN ISOLATED  
BARCHAN SAND DUNE (Virginia Univ.) 109 P  
CSCL 04B G3/47 47939  
HC \$5.50

THE INTERACTION OF UNIDIRECTIONAL WINDS  
WITH AN ISOLATED BARCHAN SAND DUNE

Sept

Technical Report  
Contract No. NGR 47-005-172

Submitted to:

NASA Scientific and Technical Information Facility  
P. O. Box 8757  
Baltimore/Washington International Airport  
Maryland 21240

Submitted by:

Mohamed Gad-el-Hak  
Assistant Professor  
Engineering Science and Systems

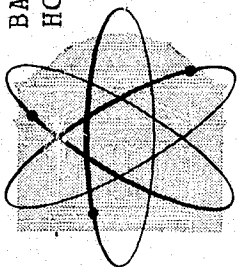
Deborah Pierce  
Research Assistant

Alan Howard  
Associate Professor  
Environmental Sciences

Jeffrey B. Morton  
Associate Professor  
Engineering Science and Systems

**SCHOOL OF ENGINEERING AND  
APPLIED SCIENCE**

RESEARCH LABORATORIES FOR THE ENGINEERING SCIENCES

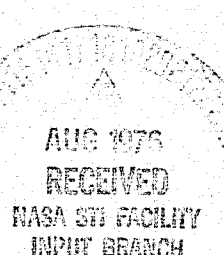


**UNIVERSITY OF VIRGINIA**

**CHARLOTTESVILLE, VIRGINIA 22901**

Report No. UVA/528035/ESS76/102

July 1976



THE INTERACTION OF UNIDIRECTIONAL WINDS  
WITH AN ISOLATED BARCHAN SAND DUNE

Technical Report  
Contract No. NGR 47-005-172

Submitted to:

NASA Scientific and Technical Information Facility  
P. O. Box 8757  
Baltimore/Washington International Airport  
Maryland 21240

Submitted by:

Mohamed Gad-el-Hak  
Assistant Professor  
Engineering Science and Systems

Deborah Pierce  
Research Assistant

Alan Howard  
Associate Professor  
Environmental Sciences

Jeffrey B. Morton  
Associate Professor  
Engineering Science and Systems

Department of Engineering Science and Systems

RESEARCH LABORATORIES FOR THE ENGINEERING SCIENCES

SCHOOL OF ENGINEERING AND APPLIED SCIENCE

and

Department of Environmental Sciences

UNIVERSITY OF VIRGINIA

CHARLOTTESVILLE, VIRGINIA

Report No. UVA/528035/ESS76/102

July 1976

Copy No. \_\_\_\_\_

## ABSTRACT

The earth's desert boundary layer is modeled in a wind tunnel. Velocity profile measurements are determined on and around a barchan dune model inserted in the roughness layer on the tunnel floor. A theoretical investigation is made into the factors influencing the rate of sand flow around the dune. Flow visualization techniques are employed in the mapping of streamlines of flow on the dune's surface. Maps of erosion and deposition of sand are constructed for the barchan model, utilizing both flow visualization techniques and friction velocities calculated from the measured velocity profiles. The sediment budget found experimentally for the model is compared to predicted and observed results reported by others. The comparison shows fairly good agreement between the experimentally determined and predicted sediment budgets; this provides encouragement for the utilization of wind tunnel simulation and friction velocity approximation in determining erosion and deposition rates due to wind action.

## TABLE OF CONTENTS

	Page
ABSTRACT . . . . .	ii
LIST OF FIGURES . . . . .	v
LIST OF SYMBOLS . . . . .	viii
<b>Chapter</b>	
1. INTRODUCTION AND BACKGROUND . . . . .	1
Introduction and Background . . . . .	1
2. THEORETICAL CONSIDERATIONS . . . . .	5
Forces on a Sand Grain in Saltation . . . . .	5
Wind Velocity Profiles above a Sand Surface; Determination of Local Friction Velocities . . . . .	18
Parameters Affecting the Sediment Budget for the Barchan Dune . . . . .	24
3. DESCRIPTION OF EQUIPMENT AND EXPERIMENTAL PROCEDURE . . . . .	31
Wind Tunnel Simulation of the Atmospheric Boundary Layer . . . . .	31
The Sand Dune Models . . . . .	36
Velocity Measurement Apparatus and Procedure . . . . .	43
The Use of Flow Visualization as a Wind Direction Indicator . . . . .	46
4. EXPERIMENTAL RESULTS . . . . .	50
Velocity Profiles around a Barchan Sand Dune . . . . .	50

Chapter	Page
Local Friction Velocities on the Barchan Dune . . . . .	71
Streamline Mapping of Barchan #1 . . . . .	73
Mapping the Sediment Budget for Barchan #1 . . . . .	80
5. SUMMARY . . . . .	91
The Interaction of Unidirectional Winds with a Barchan Sand Dune . . . . .	91
BIBLIOGRAPHY . . . . .	93
APPENDIX . . . . .	96

## LIST OF FIGURES

Figure	Page
1. Relation of Height of Rise of Grain in Saltation to Length of Grain Path . . . . .	6
2. Variation of the Threshold Velocity with Grain Size and Specific Gravity . . . . .	11
3. Observed Wind Velocity over a Dune During Saltation . . . . .	21
4. Diagram of Angles $\alpha$ and $\theta$ . . . . .	27
5. Diagram of the Angle $\gamma$ . . . . .	27
6. Schematic of the Wind Tunnel Test Section .	32
7. Turbulence Intensities at Various Downstream Locations . . . . .	34
8. Undisturbed Velocity Profiles at Various Downstream Locations . . . . .	35
9. Contour Map of Barchan #1 . . . . .	37
10. Contour Map of Barchan #2 . . . . .	38
11. Contour Map of Barchan #3 . . . . .	39
12. Schematic Grid of Profile Locations (Barchan #1) . . . . .	41
13. Perpendicular and $45^\circ$ Hotwires . . . . .	44
14. Tuft Flow Visualization Photographs of Barchan #1 . . . . .	47
15. Orientations of $45^\circ$ Hotwire . . . . .	49
16. Velocity Profiles in the Lee of Barchan #1 . . . . .	52
17. Diagram of Velocity Profiles Along Line 7 (Barchan #1) . . . . .	53
18. Velocities at $\xi = 2.54$ mm Superimposed on Height Contours for Barchan #1 . . . . .	56

Figure	Page
19. Directional Wind Pattern Derived from Velocity Profiles in the Lee of Barchan #1 . . . . .	59
20. Scaled Velocity Profiles at 5 and 10 m/s . . . . .	61
21. Comparison Between Free-Stream and Logarithmic Velocity Profiles . . . . .	63
22. Velocity Profiles at 13 crest (13 A') with Change of Wind Angle (0° to -30°) . . . . .	65
23. Velocity Profiles at 13 crest (13 A') with Change of Wind Angle (0° to 30°) . . . . .	66
24. Velocity Profiles at 2 crest (2 A') with Change of Wind Angle (0° to -30°) . . . . .	67
25. Velocity Profiles at 2 crest (2 A') with Change of Wind Angle (0° to 30°) . . . . .	68
26. Contours of Measured $u_*$ Values for Barchan #1 . . . . .	72
27. Streamline Map of Barchan #1 (From Tuft Photographs) . . . . .	74
28. Streamline Map of Barchan #1 (From Field Measurements) . . . . .	76
29. Ripple-Line Map of Barchan #1 . . . . .	77
30. Erosion and Deposition Contours for Barchan #1 (Neglecting Slope Effects) . . . . .	81
31. Erosion and Deposition Contours for Barchan #1 (Including Slope Effects) . . . . .	82
32. Map of $\tan \theta$ Values for Barchan #1 (Reference 1) . . . . .	84
33. Erosion and Deposition Contours for Barchan #1 (Including Slope Effects), Using Ripple-Lines . . . . .	85

Figure	Page
34. Erosion and Deposition Contours for Barchan #1 (From Field Observations over a Two-Week Period of Stake Exposure and Burial, Reference 1) . . . . .	87
35. Predicted Erosion and Deposition Rates for Barchan #1 . . . . .	88
36. $k'$ vs. Position on Crestline for Barchan #1 (From Field Measurements of $q$ ) . . . . .	98
37. $k'$ vs. Position on Crestline for Barchan #1 (From Wind Tunnel Measurements of $q$ ) . . . . .	99

## LIST OF SYMBOLS

A	Bagnold's constant coefficient (= 0.1 for saltation in air)
b	span
c	scaling factor
$C_D$	coefficient of drag
d	rod diameter of logarithmic grid
D	standard particle diameter
$D_p$	particle diameter
E	voltage (D.C.)
F	force
$F_f$	fluid force on a sand grain
$F_g$	gravitational force on a sand grain
g	gravitational constant
h	thickness of saltation layer
H	height of the crestline above the base of a dune
$H_e$	the effective crest height for a dune
$k'$	roughness value of surface during saltation
$l$	subscript, denotes local
L	subscript, denotes lift
m	particle mass
m	subscript, denotes maximum
O	order of magnitude
q	bulk rate of sand transport

R	drag
Re	Reynold's number
s	surface area of a spherical sand particle
t	time
u'	rms voltage
$u_*$	friction velocity = $(\tau_0/\rho_\alpha)^{1/2}$
$\bar{U}$ , U	mean wind velocity in x-direction
$\bar{U}_R$	tunnel reference speed (= 10 m/s)
$\bar{U}_x$	tunnel reference speed ( $\neq$ 10 m/s)
x,y,z	Cartesian coordinates; z is height, y is perpendicular to wind, and x is parallel
$z_o$	roughness value for a surface
$z_r$	a reference height in the wind tunnel
$\alpha$	angle of repose of a sand grain on the bed
$\gamma$	angle between the surface wind and the surface gradient
$\Gamma$	circulation
$\theta$	slope angle of the dune
$\theta'$	angle at which wind is blowing with respect to the x-axis
$\kappa$	Von Karman's constant
$\nu$	kinematic viscosity
$\xi$	angle between the mean wind and the crestline of the dune
$\xi'$	height above a surface (dune or tunnel floor)
$\rho_\alpha$	density of air

$\sigma$  density of a quartz ( $\text{SiO}_2$ ) sand grain  
 $\tau_o$  surface shear stress  
 $\omega$  angular velocity  
rel subscript, denotes relative

## Chapter 1

### INTRODUCTION AND BACKGROUND

#### 1.0 Introduction and Background

Photographs taken from the Mariner 9 spacecraft of the surface of Mars reveal the presence of eolian (wind blown) landforms closely resembling the desert dunes found on Earth. In order to study the characteristics of the atmospheric winds and surface features of Mars, it was determined that more information was needed concerning the effects of the earth's desert boundary layer winds on the formation and transport of sand dunes.

Measurements of the velocity profiles surrounding actual barchan dunes were made at a location near the Salton Sea in California [1]. The barchan dune, a crescent-shaped sand dune, was selected as an appropriate landform for study because it appears in the Mariner 9 photographs. It occurs as an isolated phenomenon and as the result of unidirectional winds convenient to simulate in a wind tunnel. The barchan is also self-preserving in shape and size over time.

A wind tunnel study was performed, wherein the earth's desert boundary layer was simulated, and scale models of the barchan dunes observed in the field were inserted. One of the models, selected on the basis that it was symmetrical and small enough to rotate through angles

of  $-30^\circ$  to  $30^\circ$  in the tunnel, was subjected to greater investigation than the others. Measurements of velocity profiles around the model yielded information about the local friction velocities on the dune, from which expressions could be derived for sand transport on and around the dune. In addition, qualitative information about the wind flow at various heights above the surface of the dune was obtained from the profiles. Streamline maps determined from hotwire measurements, flow visualization methods and measurements made in the field aided in predicting the sand flow.

The "dust bowl" erosion of the Midwest in the 'thirties stimulated a number of agriculture-related studies of wind erosion, focusing on the characteristics of particle saltation and prevention of erosion. Saltation is a method of sand transport characterized by a jumping movement of sand particles. Semi-empirical formulae were developed to give the amount of sand transported over a flat surface as a function of grain size and friction velocity.

Theoretical studies made of the forces on a sand grain in saltation were helpful in determining the factors to be considered in calculating the sediment budget for the barchan dune. Some controversy arises in determining the forces responsible for the initiation of saltation; in particular, it is not clear what role lift plays in

Experimentally determined maps of erosion and deposition of sand on the barchan dune, constructed from stream-line maps and a friction velocity contour map, are compared to a predicted map of the sediment budget (for dune equilibrium) and to a map of observed erosion and deposition for the dune. By comparing maps of the sediment budget (erosion and deposition), it was possible to determine qualitatively the accuracy of the wind tunnel simulation and the validity of the methods used in the experimental calculation of the sediment budget.

**PRECEDING PAGE BLANK NOT FILMED**

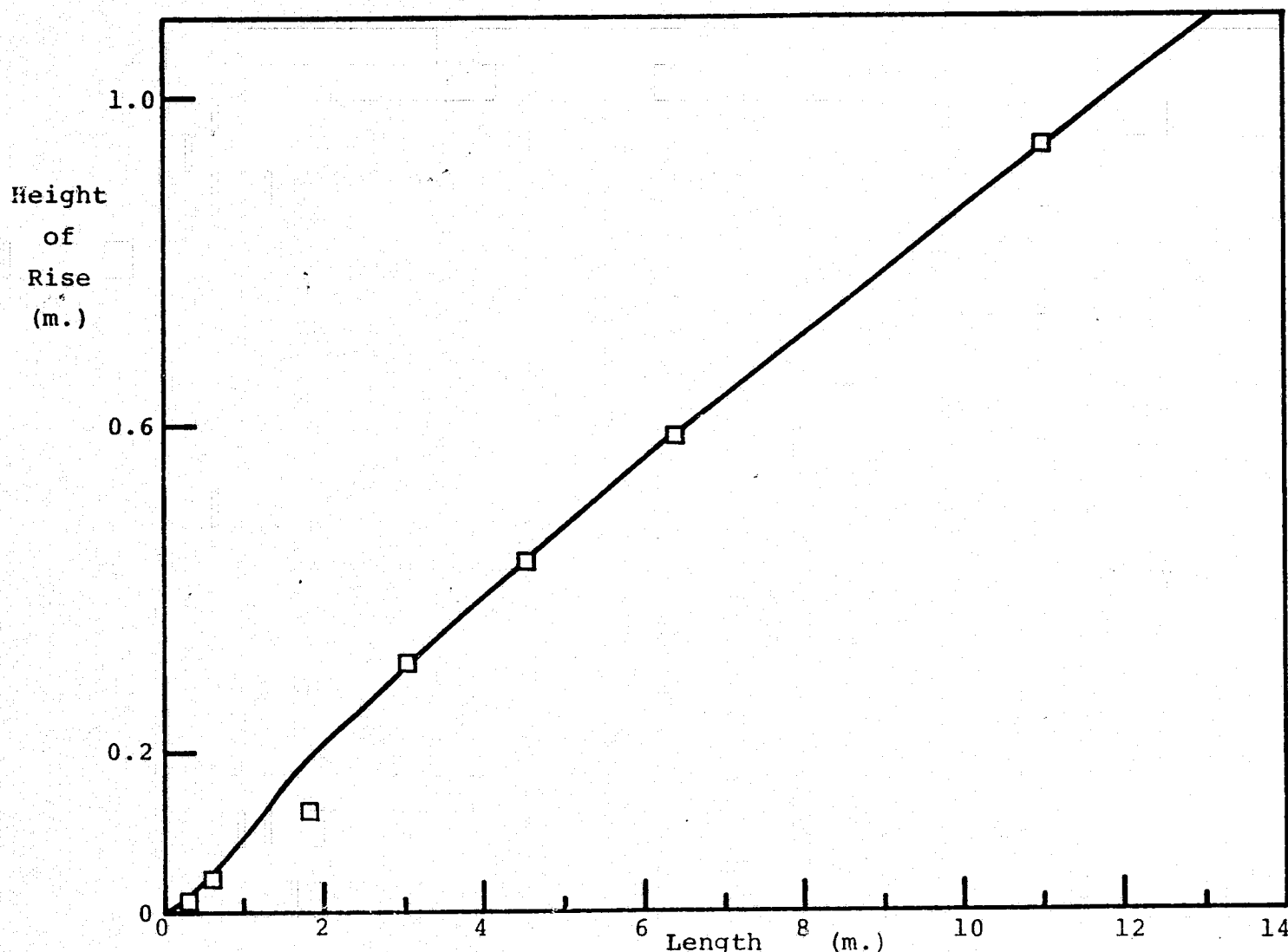


Figure 1: Relation of Height of Rise in Saltation to Downstream Distance Travelled (Chepil, W.S., "Dynamics of Wind Erosion I," Soil Science; 60: p. 312, fig. 4, 1945)

velocity of the wind increases with height, imparting horizontal momentum to the grains, so they travel a greater horizontal distance on the descent than on the ascent.

The smallest grains may sometimes be expelled by larger grains and remain aloft for longer periods of time than the larger grains; those grains are said to be in suspension. Only a fraction of a percent of the total bulk of sand grains are transported in suspension [7]. The remaining 20-25% of particles are transported by surface creep, which is characterized by a rolling motion of grains on the surface. The largest grains generally move in surface creep.

From reference 6, White et al. list several kinds of forces acting on an individual grain in saltation in a fluid medium:

- (a) the weight of the grain
- (b) drag, a force, tangential to the direction of grain motion
- (c) lift, a force, normal to the direction of grain motion, caused by the pressure distribution on the particle's surface
- (d) cohesional forces acting between individual grains
- (e) the force of overturning moment in shear flow
- (f) the Bassett force, which accounts for the effect of deviation in flow pattern from steady state

(g) the apparent mass force, which accelerates the virtual mass of the particle relative to the ambient fluid

(h) the force resulting from the effect of temperature gradients in the flow field.

For a more detailed description of these forces, see reference 9. An additional force, resulting from the fact that grains in saltation are not isolated, but interact with grains on the surface, must also be taken into account; P. Nemenyi [8] calls this force the surface force. The surface force is any normal or tangential force exerted on a grain by any other grain, excluding cohesive forces.

According to Hinze [9], the Basset force and apparent mass force are only important if the density of the fluid is equal to or greater than the density of the particle.

This is clearly not applicable to the case of sand in saltation, where the density of quartz grains is at least three orders of magnitude greater than the density of air [7]. From reference 6, the force of overturning moment in a shear flow is of importance in calculating the minimum wind speed necessary to initiate saltation (friction threshold speed), but is not important in calculating particle trajectory after initiation of motion. The effect of the overturning moment force is discussed in greater detail in section 2.2. From reference 7, cohesive forces are not generally felt to be important for

sand grains in saltation, since most of the particles in saltation are too large to allow cohesional effects to be dominant. The temperature is assumed constant for the turbulent boundary layer, so forces resulting from the effect of temperature gradients will not be considered. The remaining forces can be divided into two classifications: those responsible chiefly for initiation of the particle trajectory and those that affect the particle once it is in flight.

For grains already in flight, Bagnold singles out the forces of gravity and fluid resistance acting in a direction opposite to the relative motion of the sand particle through the fluid as being the predominant forces acting on the grain [7].

Owen [5] gives the nonlinear equations of motion of the particles (neglecting lift), once saltation has been initiated, as:

$$my + mg + R(s)\dot{y}/s = 0 \quad 2.0.1$$

$$mx - R(s)(U - \dot{x})/s = 0 \quad 2.0.2$$

where the oncoming wind blows in the x-direction and y is positive upwards. R is the drag and  $s = \{\dot{y}^2 + (U - \dot{x})^2\}^{1/2}$ .

From reference 6, the drag force, R, for a spherical particle may be expressed as a function of the relative velocity of the sand particle and the fluid and the coefficient

of drag,  $C_D$ , in the following manner:

$$R = C_D \rho_a U_{\text{rel}}^2 \frac{\pi D p^2}{8} \quad 2.0.3$$

where, for Reynold's numbers less than 100,

$$C_D = \frac{24}{Re} \left(1 + \frac{3}{16} Re\right)^{\frac{1}{4}};$$

$$\text{for } 100 < Re < 2000, C_D = 10^{0.305865(2 - \log_{10} Re)},$$

and for  $Re \geq 2000, C_D = 0.4$ . Equations 2.0.1 and 2.0.2 neglect lift as a force effective on particles after the initiation of saltation. It is unknown if lift is an important factor in determining the trajectories of sand grains; if an expression for lift,  $F_L$ , were included the lift force (to be defined later in this section), would be subtracted from the left hand side of equation 2.0.1.

The wind strength necessary to initiate saltation,  $u_{*t}$ , is a function of the grain size (Cf. Fig. 2). That a stronger threshold wind velocity is necessary to move larger grains is intuitively evident, but the fact that, for grains below a certain diameter, stronger winds are again necessary to initiate movement, requires some explanation. Below  $D_p \approx 0.1$  mm, the particles are too small to protrude above larger particles on the bed, and thus require a higher value of  $u_{*t}$  to dislodge them [10].

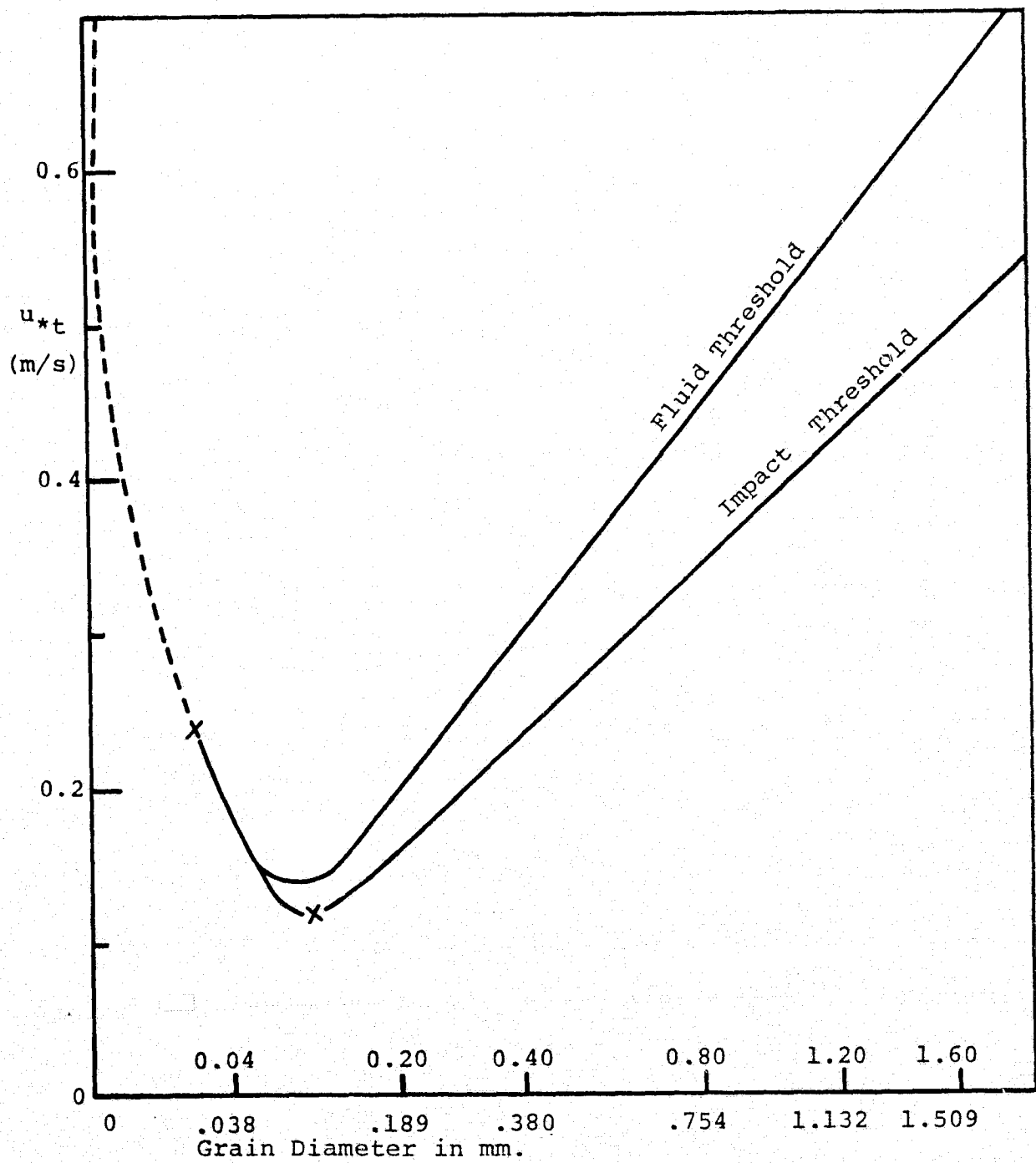


Figure 2: Variation of the Threshold Velocity with Grain Size and Specific Gravity  
 (Cepil, W.S., "Dynamics of Wind Erosion II", Soil Science, 60: p.405, 1945)

There is some controversy concerning which forces cause grains to initiate saltation. Chepil, from reference 2, discussed the forces initiating grain movement. He believed that, once saltation had been initiated, the impacts of saltating grains were responsible for continued saltation. He experimented with single sand grains on a smooth surface and noticed that a sand particle, after rolling a short distance, jumped vertically off the smooth surface, even though there were no obstructions. Combined Magnus and lift forces were suggested as a possible cause for the vertical rise.

From reference 3, Chepil and Woodruff modified Chepil's earlier views on the importance of lift in the initiation of saltation. They said that the momentum imparted to the grain by the lift force decreases rapidly with height and becomes hardly detectable a few grain diameter heights above the ground, considerably lower than the height to which many grains rise in saltation. Thus an additional vertical velocity, due to surface impact momentum transferred, must be imparted to the grain. From pressure measurements made on suspended spheres, Chepil and Woodruff conclude that lift cannot possibly be the sole factor involved in the vertical rise. The

angle at which a descending grain strikes a surface obstruction would cause the rebound to be nearly vertical even if lift did not exist. (Similarly, the angle at which a grain in surface creep strikes another grain, coupled with the drag force, should cause the initial impulse to be vertical.

Owen, from reference 5, believes that the vertical velocity of the particle is attributable to the geometry of grain impacts. He uses an order of magnitude analysis to find the ratios of lift and drag to the particle's weight and concludes that, for saltation in air, lift is at least an order of magnitude smaller than drag (assuming a spherical grain shape). For saltation in water, where  $\rho/\sigma$  is comparable to unity, lift plays an important role. (The ratio of the density of water,  $\rho$ , to  $\sigma$ , the density of silicon dioxide, is 1:2.65, if buoyance effects are neglected).

White et al., from reference 6, assume that the sand particle velocity in the initial stages of lift-off is very small; they use that assumption as a justification for using Saffman's equations for lift on a spherical particle [11]. They maintain that, since saltation occurs in laminar flow [12] where there are no velocity components normal to the surface, the occurrence of saltation must be a result of a lift force. The laminar flow stud-

ied in the case above, however, occurred in a water stream, where the density ratio between the sand particle and the fluid was comparable to unity. So although lift forces may be appreciable in the case of saltation in water, they cannot be assumed to be important to saltation in air. The use of Saffman's equations to determine the lift force on a particle in saltation in air is unjustified, since one of the limiting conditions for using the equations is that the Reynold's number,  $Re = U_{rel} D_p / v$ , must be small compared to unity. If  $u_* = 0.4$  m/s is substituted for  $U_{rel}$ , then, for a grain with  $D_p = 3 \times 10^{-4}$  m, ( $v = 1.4 \times 10^{-5}$  m<sup>2</sup>/s), the Reynold's number is 8.6.

A numerical study was performed to calculate grain particle trajectories (neglecting lift) for different values of variables  $D_p$ ,  $u_*$ ,  $z_0$  and  $v_0$ , the initial vertical velocity of the grain. Equations of motion, 2.0.1 and 2.0.2, were numerically integrated, and values for  $\ddot{x}$ ,  $\ddot{y}$ ,  $\dot{x}$  and  $\dot{y}$  were calculated for different values of time,  $t$ .  $C_D$  was made to vary as a function of the Reynold's number [13]. The height of rise and path length of the grains were tabulated for different initial conditions. Taking a typical example, it was found that a grain for which  $D_p = 0.3$  mm in a flow where  $u_* = 0.4$  m/s must have an initial vertical velocity of at least 2.5 m/s

in order to attain the height and downstream distance travelled found for the particle experimentally [14]. Thus  $Re$  for the particle is approximately equal to 50, which is obviously much greater than unity.

Using the results from the computer program mentioned above, equation 2.0.3 was evaluated to find an approximate value for the drag on a particle within a few grain diameters' height of the ground. It was found that the drag on such a particle was about  $5 \times 10^{-7}$  Newtons. The weight of the particle,  $mg$ , is equal to  $3.7 \times 10^{-7}$  Newtons. The lift due to circulation around a spinning particle is given by:

$$F_L = \rho_a U \Gamma \quad 2.0.4$$

where  $\rho_a$  is the density of air,  $U$  is the velocity in the  $x$ -direction at a particular height, and  $\Gamma$  is the circulation. The lift, drag and weight were calculated for  $u_*$  equal to 0.4 m/s, a particle diameter of 0.3 mm and  $z_0$  equal to 0.08 mm. The circulation,  $\Gamma$ , is defined as follows:

$$\Gamma = \int \bar{U} \cdot d\bar{s} \quad 2.0.5$$

where  $\bar{s}$  is a line element on the spherical sand particle. The expression for the circulation must be integrated over the sphere, resulting in an equation for the lift force as follows:

$$F_L = 2\pi \rho_a \bar{U} \omega R_m^2 \int_{-R}^R \cos^2\left(\frac{\pi b}{2R_m}\right) db \quad 2.0.6$$

where  $R_m$ , the radius of the sphere is 0.15 mm, and  $\omega$  is the angular velocity of the particle. Integrating:

$$F_L = 2\pi\rho_a \bar{U}\omega R_m^3 \quad 2.0.7$$

Values for  $\bar{U}$  and  $\omega$  are calculated using a logarithmic velocity profile (equation 2.1.2) and the fact that  $\bar{U} = \omega R_m$ . When these values, and values for  $\rho_a$  and  $R_m$  are inserted, the value for the lift force is found to be  $6.84 \times 10^{-8}$  Newtons. Thus lift on a spherical particle is an order of magnitude less than either the drag or the weight. All studies that have been made of the forces on sand grains assume a spherical grain. Since, in particular, lift forces would vary greatly depending on the shape of the particle in saltation, an investigation ought to be made of the forces on different shaped sand grains.

In conclusion, there are two forces that predominate in the saltation of a spherical sand grain once the grain has been ejected: the fluid resistance (drag) and gravity. The initial vertical velocity of (spherical) particle ejection is provided chiefly by the momentum transfer that occurs during surface impacts between grains. The descending grain in saltation possesses momentum acquired from drag and previous impact. If it can be assumed that spherically-shaped sand grains are capable of initiating saltation, they must acquire an initial vertical

momentum from some source other than lift; one hypothesis is that they roll a short distance in surface creep as a result of drag, then rebound against surface obstructions vertically, beginning saltation. The nature and magnitude of lift forces on actual sand grains is unknown, but it is probable that lift plays an important role in the saltation of irregularly shaped grains and may not prove to be negligible, as it is when a spherical grain shape is assumed [15].

## 2.1 Wind Velocity Profiles above a Sand Surface;

### Determination of Local Friction Velocities

One of the first steps in the determination of erosion and deposition patterns at various locations on a barchan dune is finding the local friction velocities at these locations, since the rate of sand flow is a function of the local friction velocity. Values for friction velocity may be determined from velocity profiles measured above the locations in question.

Velocity profiles above a flat sandy surface have been measured by many experimentalists, and two types have been observed: profiles above stationary sand surfaces and profiles above drifting sand surfaces.

From reference 7, Bagnold writes the logarithmic velocity profile equation for a stationary sand surface (where saltation has not occurred):

$$U = 5.75 u_* \log_{10} \frac{z}{z_0} \quad 2.1.1$$

where  $U$  is the fluid velocity at height  $z$  above the surface with a roughness constant  $z_0$  and friction velocity  $u_* = \sqrt{\tau_0/\rho_a}$ , where  $\tau_0$  is the surface shear stress and  $\rho_a$  is the density of air. An alternate form of equation 2.1.1 is

$$U = \frac{u_*}{\kappa} \ln \frac{z}{z_0}$$

2.1.2

where  $\kappa$ , the von Karman constant is equal to 0.4.

When the friction velocity is sufficiently large, the sand particles start to move. Bagnold defines two different threshold friction velocities initiating grain movement. The fluid threshold is the friction velocity that the fluid must attain before the grains start to move without any other upwind interference. The fluid threshold varies with the grain diameter as follows:

$$u_{*t} = A \sqrt{\frac{\sigma - \rho}{\rho} g D_p}$$

2.1.3

where  $A$  is a constant coefficient which is 0.1 for saltation in air; Zingg [16] and Chepil [17] found the same value for  $A$  experimentally.  $\sigma$  and  $\rho$  are the grain and air densities, respectively, and  $D_p$  is the particle diameter. If oncoming grains from upwind provide an initial source of kinetic energy, a lower threshold friction velocity is required to initiate saltation; this is the impact threshold. For grains where  $D_p \geq 0.25$  mm (0.25 mm is the size of fine dune sand grains), the impact  $u_*$  is given by equation 2.1.3, where  $A = 0.08$ . Chepil, from reference 10, questions the relevance of adding kinetic energy to determine a separate threshold velocity. Recog-

nizing the difficulty in determining visually the actual velocity at which saltation begins, he defines "minimal" and "maximal" threshold friction velocities.

Once saltation is initiated, the velocity still varies as the log of the height, but the velocity rays pass through a new fixed focus at height  $k'$ , which is of the order of magnitude of the surface ripples formed by the sand flow [Cf. Figure 3]. The resulting equation for the wind velocity  $U_s$ , where  $U_s$  is the wind velocity at a height  $z$  for the case of saltating sand, is

$$U_s = \frac{u_*}{\kappa} \ln \frac{z}{k'} + U_t \quad 2.1.4$$

where  $U_t$  is the impact threshold velocity defined by

$$U_t = \frac{u_* t}{\kappa} \ln \frac{k'}{z_0} \quad 2.1.5$$

( $u_* t$  is the impact threshold friction velocity defined in equation 2.1.3). Experiments performed by Zingg indicate that, for wind over drifting sand surfaces,  $\kappa$  is more closely approximated by  $\kappa = 0.375$ , but Horikawa and Shen [18] concluded that there is not sufficient evidence to deviate from a value of  $\kappa = 0.4$ .

For average dune sand of mixed grain size ( $D_p$  varying from 0.1 mm to 1 mm), Bagnold estimates values of  $U_t = 4$  m/s and  $k' = 1$  cm. These values are supported by Zingg's experimentally determined approximations of  $k' = 10 D_p$  and  $U_t = 20 D_p$ ;  $k'$  and  $D_p$  are in millimeters,

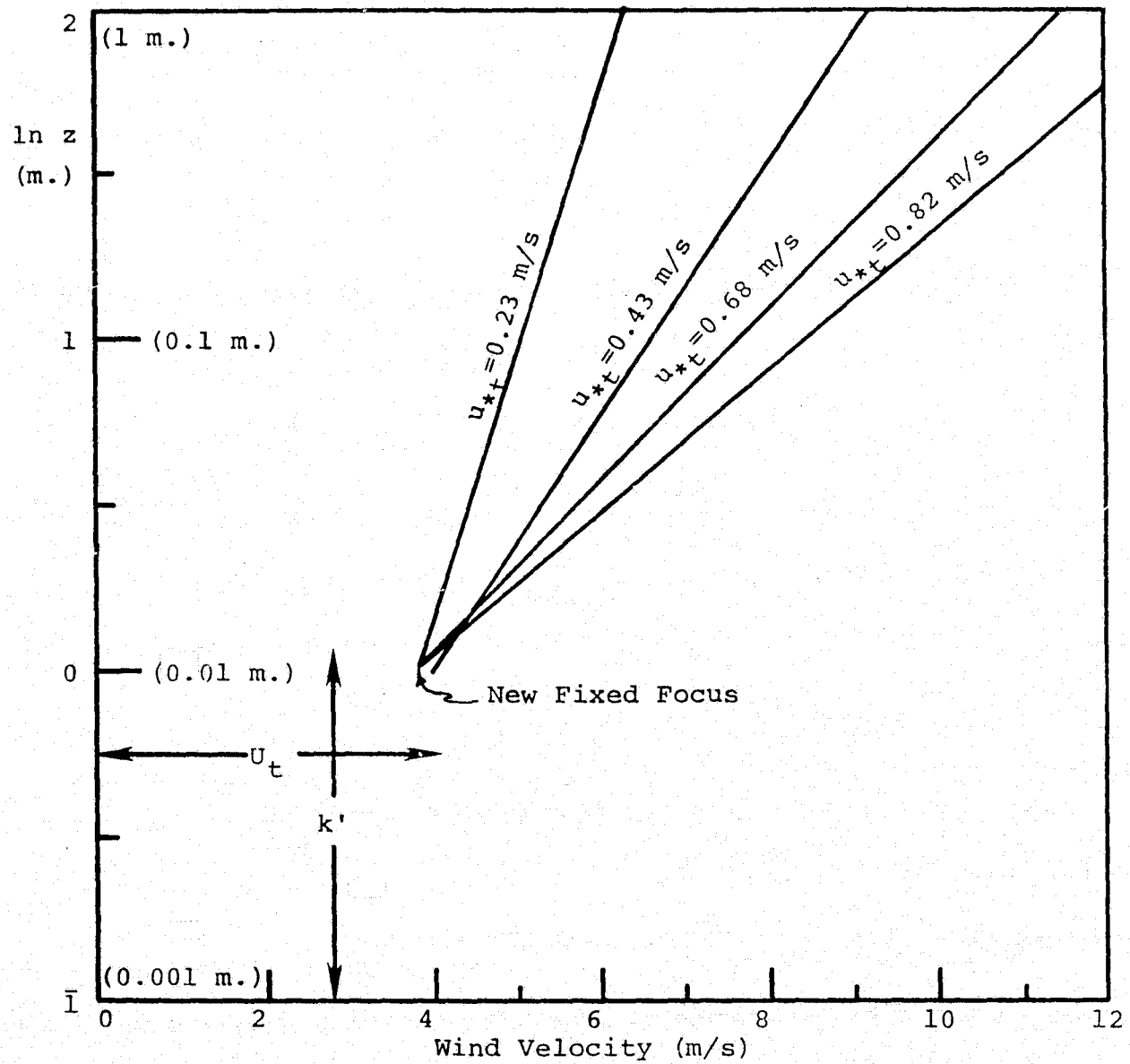


Figure 3: Observed Wind Velocity over a Dune During Saltation  
 (Bagnold, R.A., The Physics of Blown Sand and Desert Dunes, Methuen, p.82, fig.25, 1941)

and  $U_t$  is given in miles per hour. Local values of the friction velocity are determined from the velocity profiles at different locations on and around a barchan dune using equation 2.1.4 and substituting in Bagnold's values for  $U_t$  and  $k'$ . Values for  $U$  were obtained in the wind tunnel at a height  $z = 2.54$  mm (for each location), which, when multiplied by a factor of 315 (used to scale field dimensions to wind tunnel dimensions), is equal to a height of 0.8 m in the desert. The velocity is multiplied by a scaling factor,  $C$ , in order to normalize tunnel velocities to different assumed wind strengths at a height  $z = 0.8$  m upstream with respect to the dune in the desert. This may be done because results from Chapter 4 show that the flow is Reynold's number independent for the values of Reynold's numbers at which the measurements were performed. From velocity profiles measured in the tunnel at a tunnel reference speed  $U_R = 10$  m/s, the mean velocity found upstream of the dune model at  $z = 2.54$  mm is 4.5 m/s. Thus, in order to normalize all velocity values to an upstream velocity at that height of, for example, 10 m/s, a scaling factor  $C = 2.22$  would be used.

Making the appropriate substitutions, the equation for the local friction velocity is

$$u_* = 0.4 \left[ \frac{cU - 400}{\ln 80} \right] \quad 2.1.6$$

The method described above for determining the friction velocity assumes a logarithmic profile between the lowest point of measurement (2.54 mm) and the point ( $U_t$ ,  $\ln k'$ ) through which the velocity curves pass during saltation. For velocity profiles over a curved surface, the assumption is not strictly true and must be taken as only an approximation.

## 2.2 Parameters Affecting the Sediment Budget for the Barchan Dune

From equations in section 2.1, an expression for the local friction velocity was derived from velocity profiles measured in the wind tunnel, where values were assigned to  $k'$  and  $U_t$ . The local friction velocities thus determined can now be used to model the sediment budget for the dune. For a flat sandy surface, the local rate of sand transfer,  $q$ , is a function of the local friction velocity and the grain diameter.

From reference 7, Bagnold's equation for  $q$ , the mass of sand transported per unit time per unit width, as a function of  $u_*$ ', the friction velocity for moving sand over a flat surface, is:

$$q = c \sqrt{\frac{D_p}{D}} \frac{\rho}{g} u_*'^3 \quad 2.2.1$$

where  $c$  is a dimensionless, experimentally determined constant ( $C = 1.8$  for naturally graded sand of the type found on desert dunes, and  $C = 1.5$  for uniform sand grains where  $D_p = 0.25$  mm). The particle diameter is denoted by  $D_p$ ,  $D$  is a standard particle diameter ( $D = 0.25$  mm), and  $\rho$  is the density of air.

Equation 2.2.1 is used to determine the rate of sand flow at the crest of the barchan model. The crestline of the dune is the line at which the slope changes abruptly.

The slip face is in the lee of the crest and the leading edge is just upstream of it. In general, the flow separates at the crest and forms a reverse circulation at the slip face [19].

For the dune to be self-preserving, it must be in equilibrium; that is, all parts of the dune must have the same rate of translation in the direction of the mean wind and the height of the dune must remain constant. From reference 1, it can be shown that at the crest, the direction of sand transport closely follows the local wind [Cf. Appendix A]. In discussing the rate of sand flow over the dune, the emphasis up to this point has been placed on the effects of the local friction velocity on  $q$ . The barchan dune has a sloping surface; the effects of the slope angle,  $\theta$  (cf Figure 4), on  $q$  must be investigated. Because of the surface slope, gravity no longer acts in a direction normal to the surface; particles initially moving will possess a downslope component of motion. Coarse particles travelling in surface creep are probably affected more than any other particles by surface slope. From reference 1, some particles very close to the dune base may be deflected by as much as  $30^\circ$  down-slope with respect to the direction of the surface wind. According to Bagnold (reference 7), the coarsest particles generally determine ripple formation; thus surface slope

effects may be responsible for deviations measured between the local surface wind and the normal to the ripple strike at various locations.

Bagnold [20] modifies the equation for the role of sand transport as a function of friction velocity to take into account local variation in the gravity slope as follows:

$$q = c \sqrt{\frac{Dp}{D}} \frac{\rho}{g} \frac{u_*'^3}{\cos\theta(\tan\alpha - \tan\theta)} \quad 2.2.2$$

where all variables are the same as in equation 2.2.1,  $\alpha$  is the angle of repose of the grain on the bed, and  $\theta$  is the surface slope angle [Cf. Figure 4]. The slope angle also affects the threshold velocity,  $U_t$ , of the sand particles. From reference 7, saltation occurs when  $F_f/F_g > \tan\alpha$  where  $F_f$  and  $F_g$  are the fluid and gravitational forces, respectively, on the grain.

$$F_f = \beta' \rho u_*'^2 Dp^2 \quad 2.2.3$$

where  $\beta'$  is an experimentally determined dimensionless coefficient which depends on the turbulent fluctuations in the flow, the drag per unit area of the fluid on the grain and the height at which the drag force acts.

$$F_g = \frac{\pi}{6} Dp^3 (\sigma - \rho) g \frac{1}{2} \quad 2.2.4$$

and

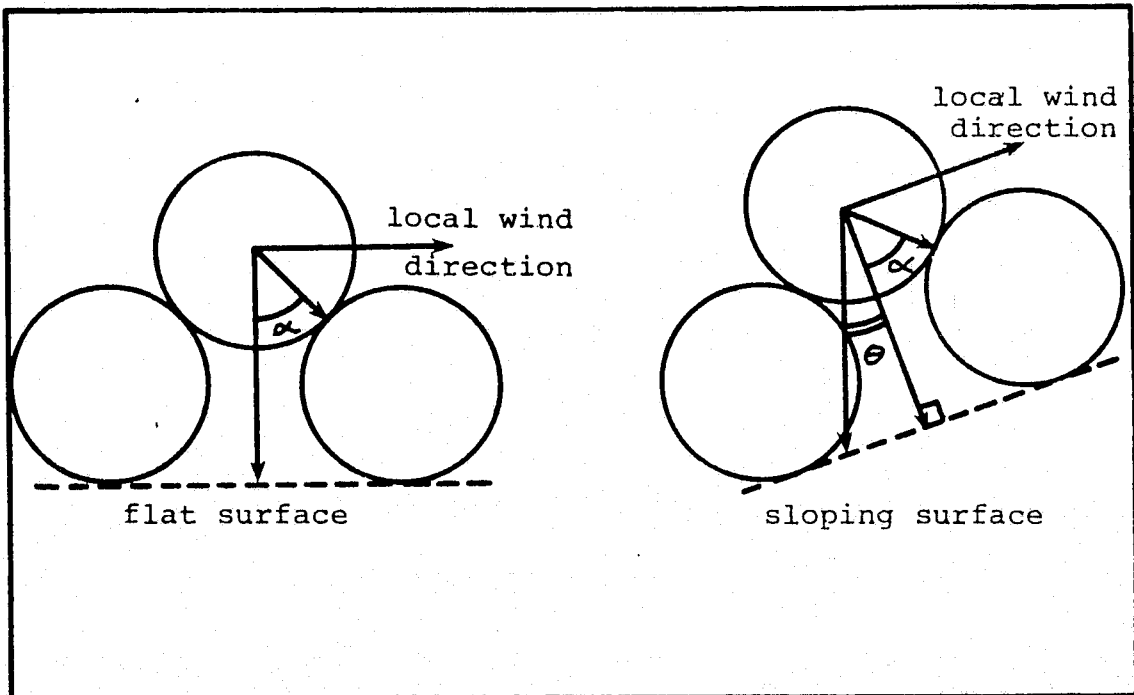


Figure 4: Diagram of Angles  $\alpha$  and  $\theta$

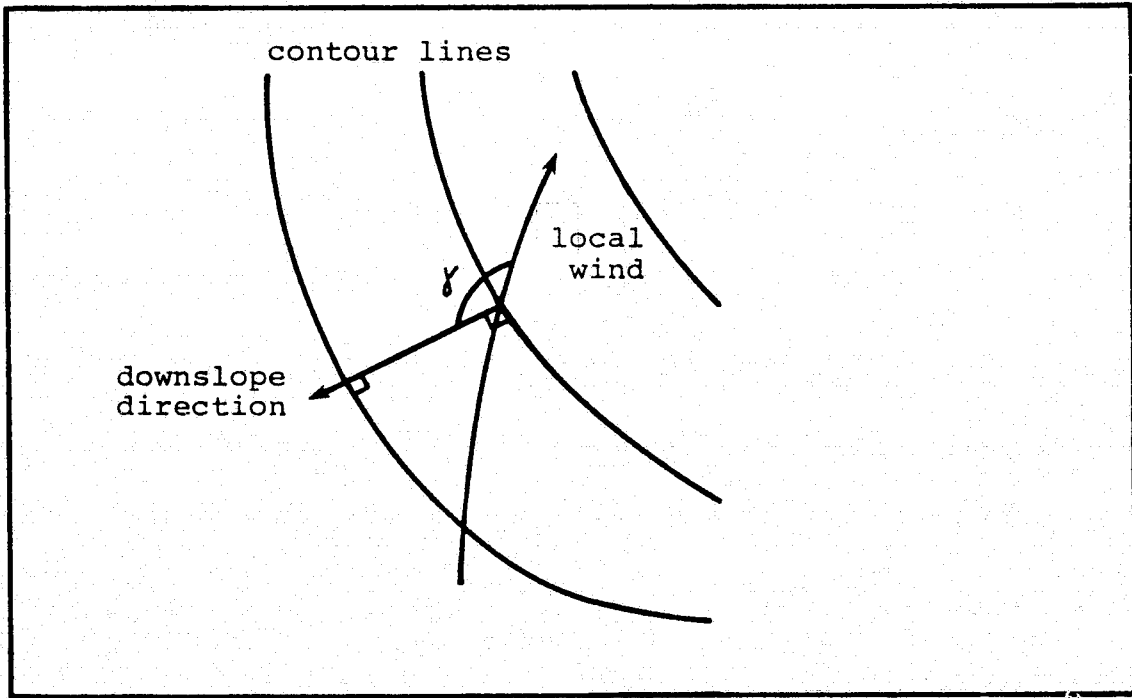


Figure 5: Diagram of the Angle,  $\gamma$

At the initiation of particle movement.

$$\frac{F_f}{F_g} = \tan\alpha = \frac{\beta' \rho u_*^2}{\frac{\pi}{12} D_p (\sigma - \rho) g} \quad 2.2.5$$

From reference 1, if surface slope effects are taken into account,  $\tan\alpha$  must be replaced by the function below:

$$\frac{F_f}{F_g} = \sqrt{\tan^2\alpha \cos^2\theta - \sin^2\theta \sin^2\gamma - \cos\gamma \sin\theta} \quad 2.2.6$$

where  $\alpha$  and  $\theta$  are defined above and  $\gamma$  is the angle between the surface wind and the surface gradient [Cf. Figure 5].

Equating 2.2.5 and 2.2.6, an expression for  $u_*$  at the initiation of grain movement is easily derived:

$$u_* = \sqrt{\frac{\pi D_p (\sigma - \rho) g}{12 \beta' \rho} \left[ \sqrt{\tan^2\alpha \cos^2\theta - \sin^2\theta \sin^2\gamma - \cos\gamma \sin\theta} \right]} \quad 2.2.7$$

From equation 2.1.2, an expression for the local threshold velocity  $U_{tl}$  is obtained and is inserted into equation 2.1.6 to yield a new value of  $u_*$  for each location. The adjusted  $u_*$  values are used in equation 2.2.2 to obtain the local rate of sand transport.

The orientation of the dune with respect to the mean wind affects both direction and quantity of sand transport at various locations on the dune. The equation used in Appendix A to find  $q$  for equilibrium at the crest includes

the angle,  $\xi$ , between the mean wind and crestline. Values for  $\xi$  are measured in the field.

Two other factors that influence  $q$  are the lag effect and the effect of variation of grain diameter. When the local friction velocity at a given location, say,  $\ell_1$ , changes, the amount of sand ejected into saltation changes also. Thus the amount of sand transported to a second location, say  $\ell_2$ , downstream of  $\ell_1$  depends, to an extent, on what takes place at  $\ell_1$ . This "lag" effect should take place over a distance of the order of one path length of the grains in saltation, where the path length is the downstream distance travelled by a grain in a single jump. The path length varies from a few centimeters to a meter. Thus the concentration,  $q$ , of sand initially arriving at a particular location should be determined by what is happening at various distances upstream. The grain size,  $D_p$ , varies with different locations on the dune. As yet, this factor has not been taken into account in calculating the sediment budget on the dune; instead, a uniform grain size of 0.25 mm has been assumed. From equation 2.2.1, however, it is clear that grain size affects the sand transport rate. To account for grain size effects, an accurate map of the distribution of  $D_p$  on a barchan dune would be required.

In a procedure more fully described in Chapter 4, streamline maps of barchan #1 are drawn and "cells" of approximately equal area are marked off between streamlines. Values for the parameters described above that affect  $q$  are found from field and wind tunnel measurements and are tabulated for locations at the center of each cell. A computer program provides adjusted values of  $q$  for each cell when different combinations of parameters are taken into account. The effects of lag on  $q$  are computed for different assumed particle path lengths. The resulting erosion and deposition rates are compared to erosion rates calculated for self-preservation of the sand dune.

## Chapter 3

### DESCRIPTION OF EQUIPMENT AND EXPERIMENTAL PROCEDURE

#### 3.0 Wind Tunnel Simulation of the Atmospheric Boundary Layer

Techniques that have been developed to simulate the atmospheric boundary layer were adapted for the experiment to produce flow over a desert surface [21]. The facility used for the simulation of a neutral desert boundary layer is an open return, subsonic wind tunnel with a test section 7.92 m long, 0.6 m wide and 0.61 m high (Cf. Figure 6). The air in the tunnel is initially forced through a contraction with a ratio of 22:1.

For a neutrally stable atmosphere, the desired mean velocity profile near the ground (where Coriolis effects may be neglected) may be written as

$$U(z) = \frac{u^*}{\kappa} \ln \frac{z}{z_0} \quad 3.0.1$$

where  $u^*$  is the friction velocity ( $U = \sqrt{\frac{\tau_0}{\rho}}$ ,  $\tau_0$  is the shear stress at the surface and  $\rho$  is the density of air),  $\kappa$  is the von Karman constant ( $\approx 0.4$ ) and  $z_0$  is the roughness height [6,22]. A variable rod grid (rod diameter,  $d$ , is 19 mm) produces, in conjunction with the appropriate roughness element fastened to the floor, the desired velocity

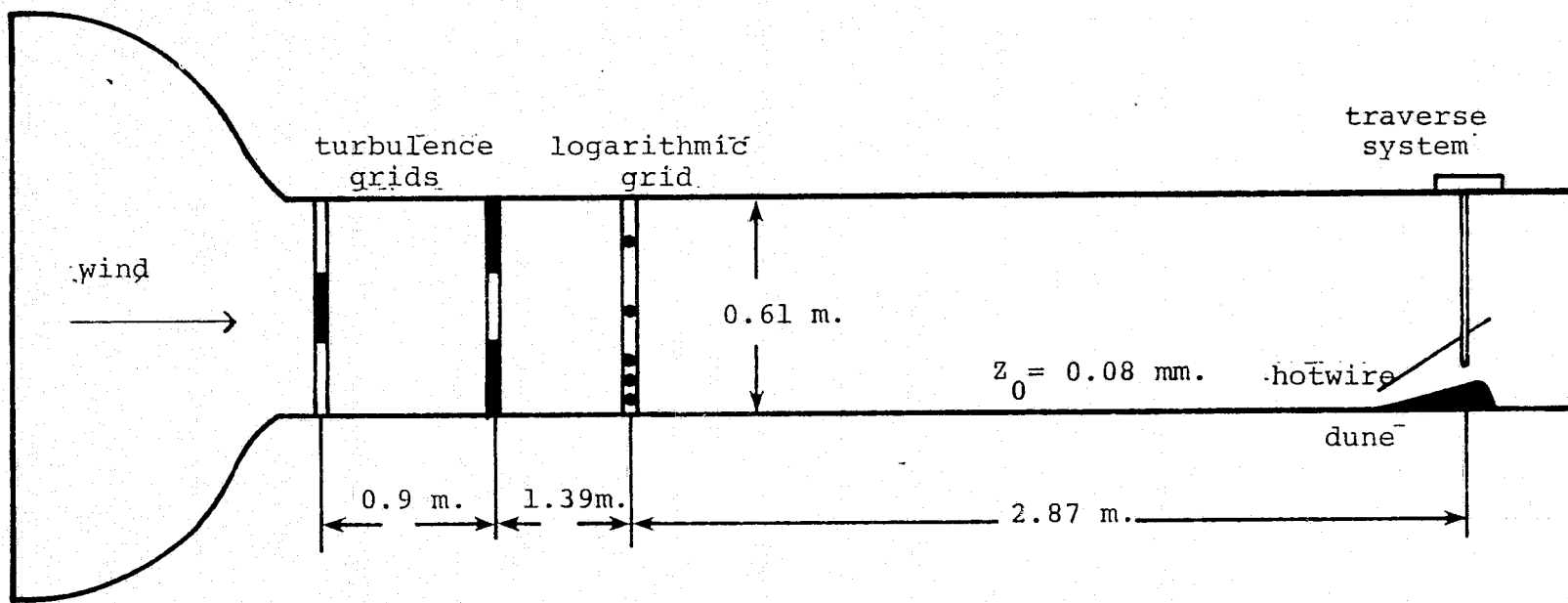
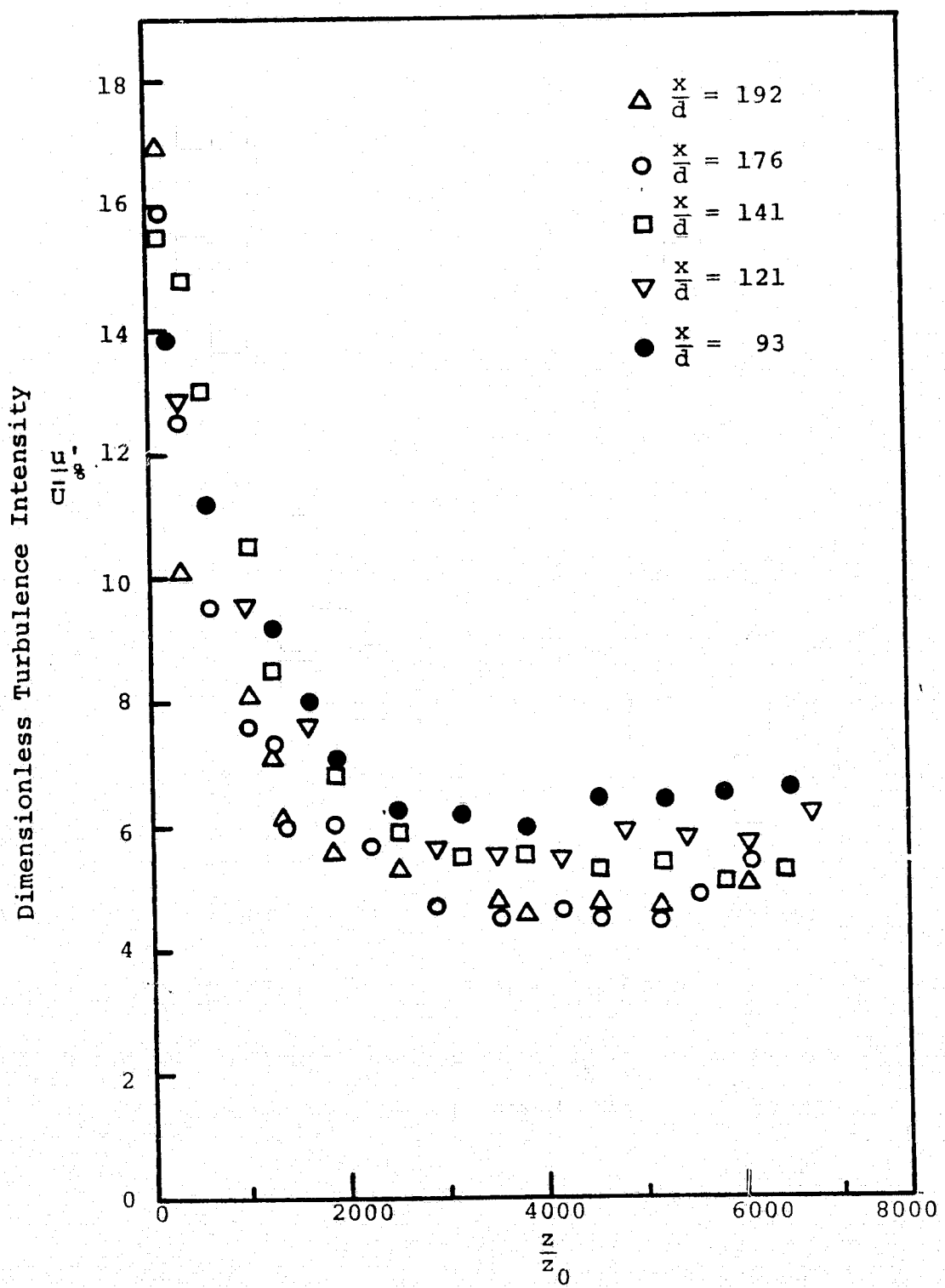


Figure 6 : Schematic of the Wind Tunnel Test Section

profile corresponding to the  $z_0$  found for saltating sand [1]. The roughness element used is 20-3½ grid silicon carbide sandpaper. From reference 21, two grids inserted at intervals upstream with respect to the rod grid produce turbulence intensities similar to those found in the earth's atmosphere. Figure 7 is a plot of the turbulence intensity profiles.

The scaling factor used in designing the experiment is 315:1. Thus the lowest 190 m of the atmospheric surface layer is represented by the tunnel height of 0.6 m and a  $z_0$  of 25.2 mm in the atmosphere is simulated by a  $z_0$  of approximately 0.08 mm in the tunnel. A semi-logarithmic plot (Cf. Figure 8) of the mean velocity profiles taken at different intervals ( $x$ ) downstream with respect to the rod grid shows good agreement with equation 3.0.1. The wind tunnel simulation of the atmospheric boundary layer compares well with naturally grown boundary layers in other wind tunnels [22,23,24,25].



Nondimensionalized Distance Above the Tunnel Floor

Figure 7: Turbulence Intensities at Various Downstream Locations

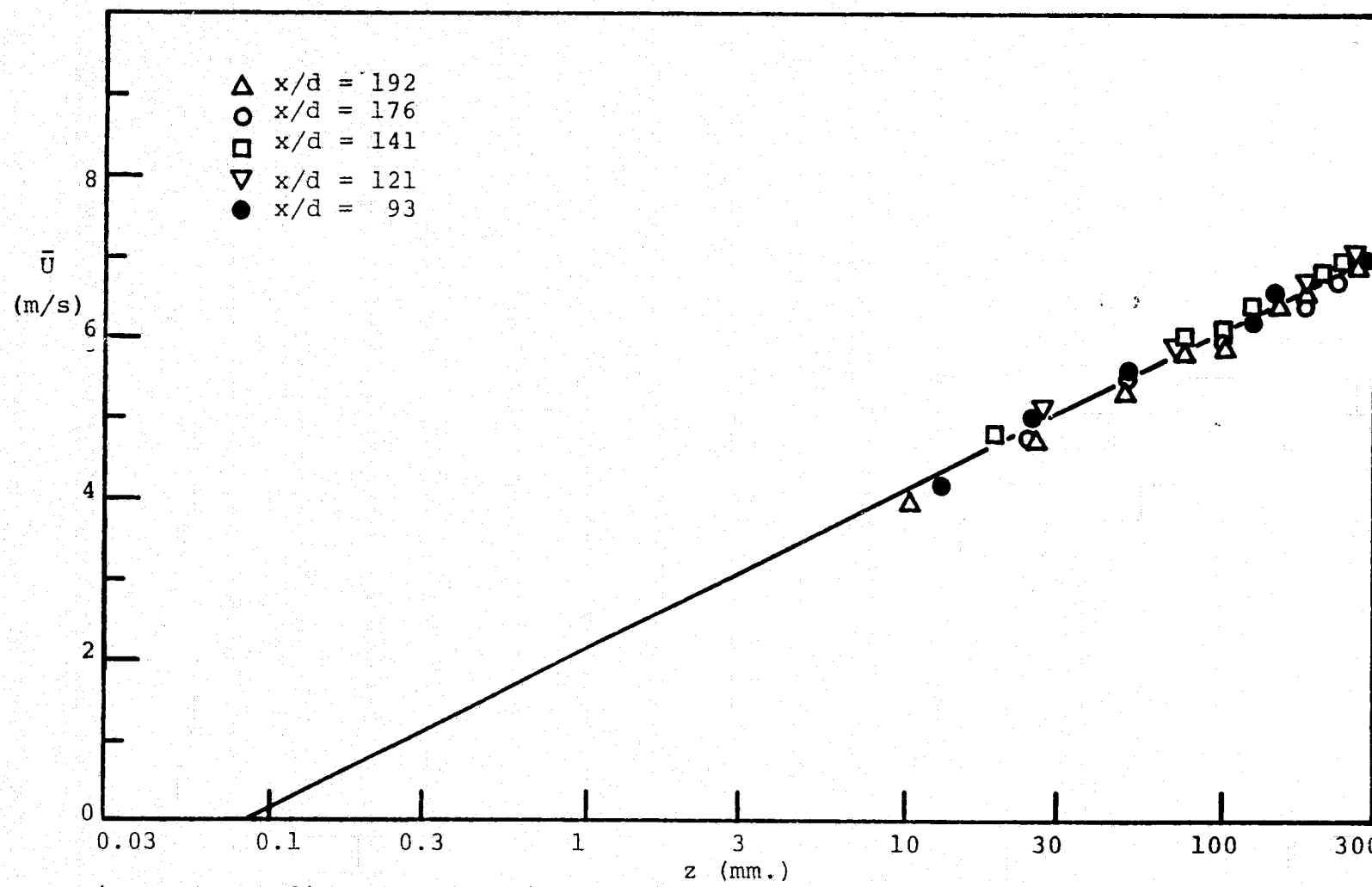


Figure 8: Undisturbed Velocity Profiles at Various Downstream Locations

### 3.1 The Sand Dune Models

Velocity profiles are measured around three different barchan dune models, which are scale models of real dunes existing near the Salton Sea in California. In the field, the dunes were surveyed and contour maps were drawn [1]. Velocity profiles were measured, using cup anemometers, at various points on the dunes, with special emphasis placed along the crestlines. Also, maps were made showing the ripple marks, slope gradient, crestline strike and slope curvature for each dune.

The models, made from the contour maps, which will be labelled barchan #1, #2 and #3 for convenience, differ in some respects. Barchan #1 [Cf. Figure 9] is about 360 mm long and 310 mm wide (across the wing-tips), barchan #2 [Cf. Figure 10] is 430 mm long and 330 mm wide and barchan #3 [Cf. Figure 11] is 340 mm long and 200 mm wide. Barchans #1 and #2 possess a similar shape with symmetrical wings, indicating laterally uniform upwind sand transport, but barchan #3 is skewed (having one wing substantially dwarfed), the result of an uneven sand supply upwind (from references 6, 7).

In the field, most of the measurements were made around the dune corresponding to barchan #1, so the most detailed set of profiles is determined for barchan #1 in

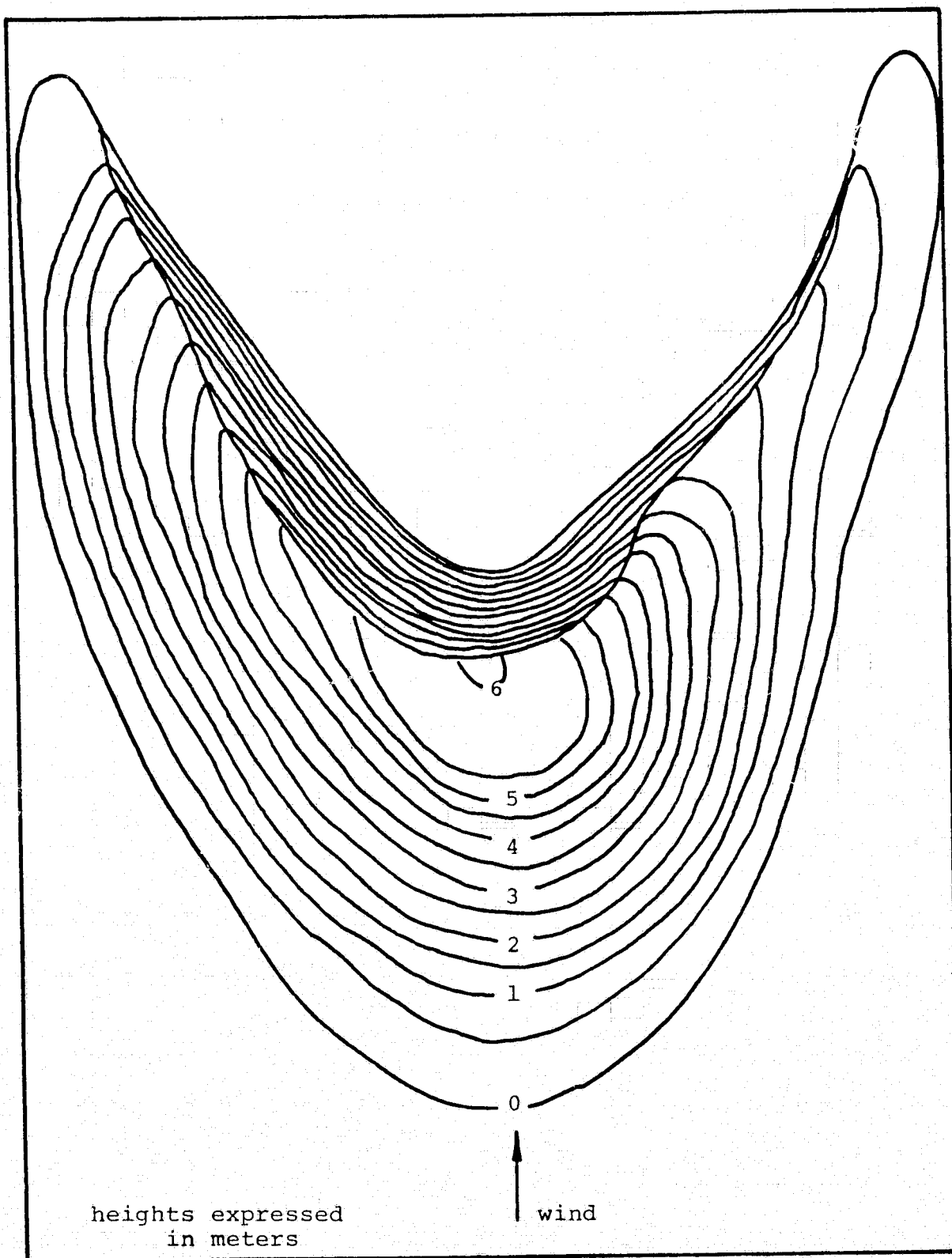


Figure 9: Contour Map of Barchan #1

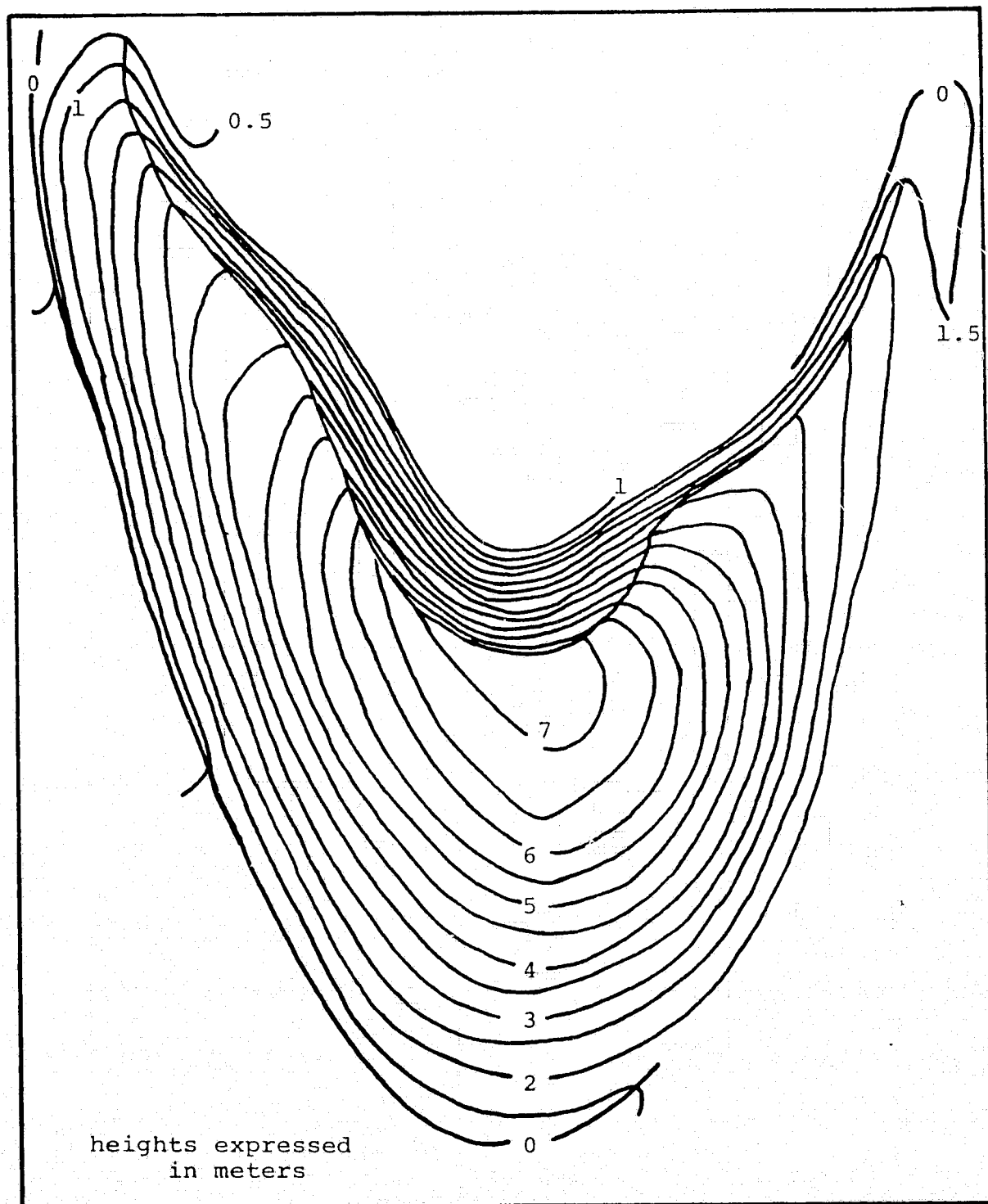


Figure 10: Contour Map of Barchan #2

the tunnel. Barchan #1 also has symmetrical wings, and its dimensions are such that any effects from the warped walls of the tunnel did not interfere with velocity profiles measured on the wings (the effects of the wind tunnel walls were determined with a pitot tube; velocity readings were determined laterally at the position where the dune models were later inserted). Barchan #2 cannot be rotated through large angles (to measure effects of multidirectional winds) because it is so large that the tunnel's wall effects, which extend about 70 mm from each wall, do interfere with mean velocity readings on the wings.

The dune models are carved from layers of balsa wood, with each layer corresponding to a height contour on the map. They are sanded to a smooth, continuous surface and spray-painted. The models are embedded into the floor roughness at a location  $151 d$  ( $d$  = rod diameter) downstream of the rod grid. Barchan #1 is mounted on a disk that can be rotated through designated angles to simulate change of wind direction. Figure 12 shows the locations at which vertical velocity profiles are determined on barchan #1. Line 7 is the center line of the dune and, in the case of winds impinging from  $0^\circ$ , is aligned with the axial direction of the tunnel and thus with the freestream flow.

the tunnel. Barchan #1 also has symmetrical wings, and its dimensions are such that any effects from the walls of the tunnel did not interfere with velocity profiles measured on the wings (the effects of the wind tunnel walls were determined with a pitot tube; velocity readings were determined laterally at the position where the dune models were later inserted). Barchan #2 cannot be rotated through large angles (to measure effects of multidirectional winds) because it is so large that the tunnel's wall effects, which extend about 70 mm from each wall, do interfere with mean velocity readings on the wings.

The dune models are carved from layers of balsa wood, with each layer corresponding to a height contour on the map. They are sanded to a smooth, continuous surface and spray-painted. The models are embedded into the floor roughness at a location  $151 d$  ( $d$  = rod diameter) downstream of the rod grid. Barchan #1 is mounted on a disk that can be rotated through designated angles to simulate change of wind direction. Figure 12 shows the locations at which vertical velocity profiles are determined on barchan #1. (The profiles were measured, for the most part, at the intersections of lines 1-13 with lines A, B and C.) The crest of the dune, which coincides with line A in the area to the right of line 9, is indicated by the heavy dotted line. Point  $\alpha$  occurs at the intersection of lines 1-13.

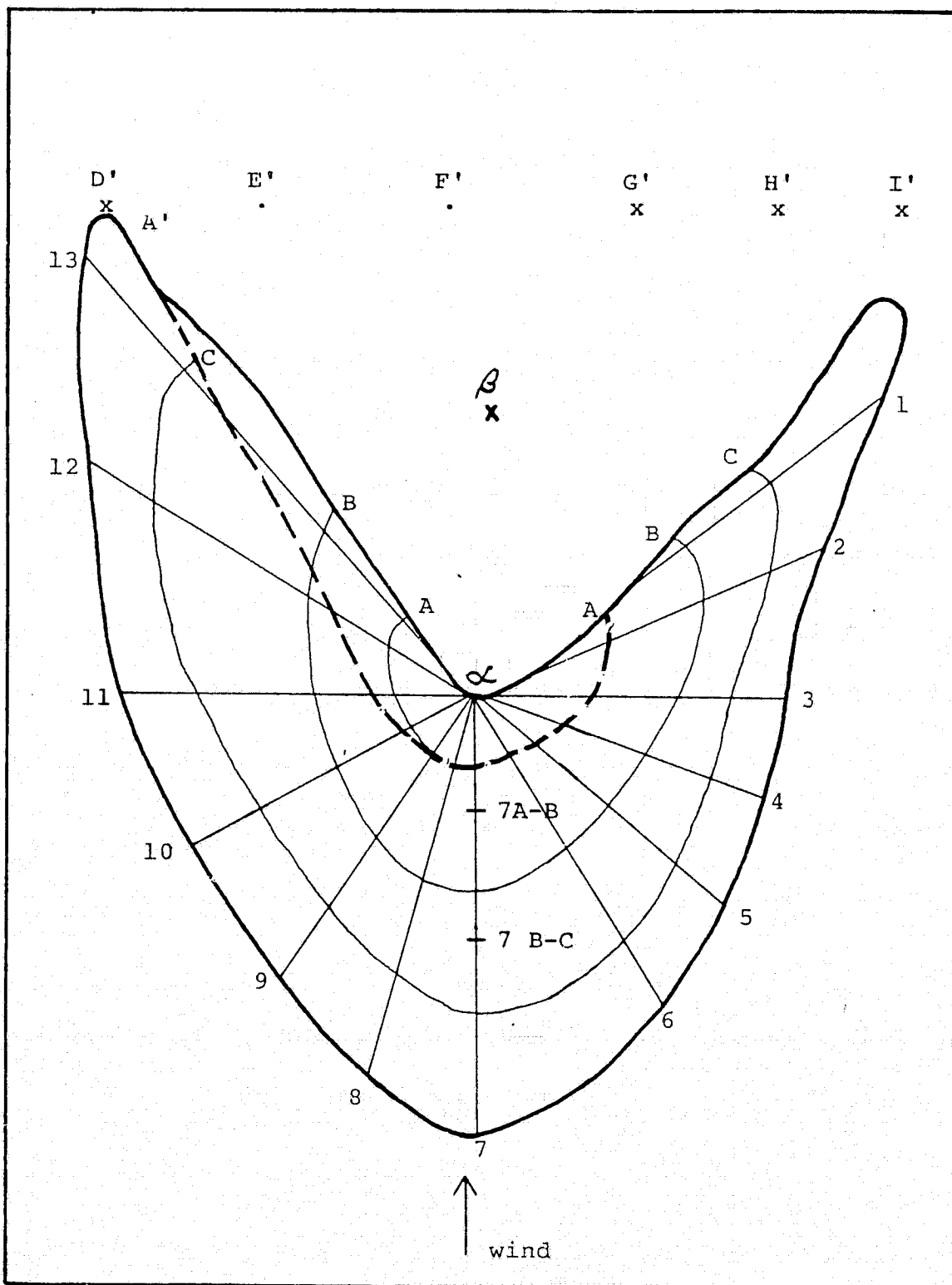


Figure 12: Schematic Grid of Profile Locations (Barchan #1)

B, D', E', F', G', H' and I' are points at which velocity profiles are measured in the lee of the model. Line 7 is the center line of the dune and, in the case of winds impinging from  $0^\circ$ , is aligned with the axial direction of the tunnel and thus with the freestream flow.

### 3.2 Velocity Measurement Apparatus and Procedure

Mean velocity profiles and fluctuating components are measured with a miniature hotwire probe connected to a constant temperature anemometer. The overheat ratio for the hotwire is 1.6 times the probe resistance. The signal is fed through a linearizer and conditioned by an auxiliary unit with high and low pass filters and a nulling circuit which zeroes the mean voltage. D.C. voltage is measured using a digital voltmeter with a variable damping control which is kept at  $t = 10$  seconds to average the u-velocities.

The hotwire is positioned with a traversing system suspended from the tunnel ceiling, and it can be moved in the x, y and z directions; the traverse mechanism is accurate to 0.5 mm in all directions. Two kinds of miniature probes are used (Cf. Figure 13). The first type, which is designed with the sensitive element perpendicular to the prongs so that the probe support is horizontal and parallel to the x-axis, is used for measuring profiles on the dune's crest and on the lee side of the crest. The second type is a  $45^\circ$  probe (the sensitive element is fastened to the prongs at an angle of  $45^\circ$ ) and is supported at an angle of  $45^\circ$  with respect to the z-direction so that the sensitive element is perpendicular to the wind; the  $45^\circ$

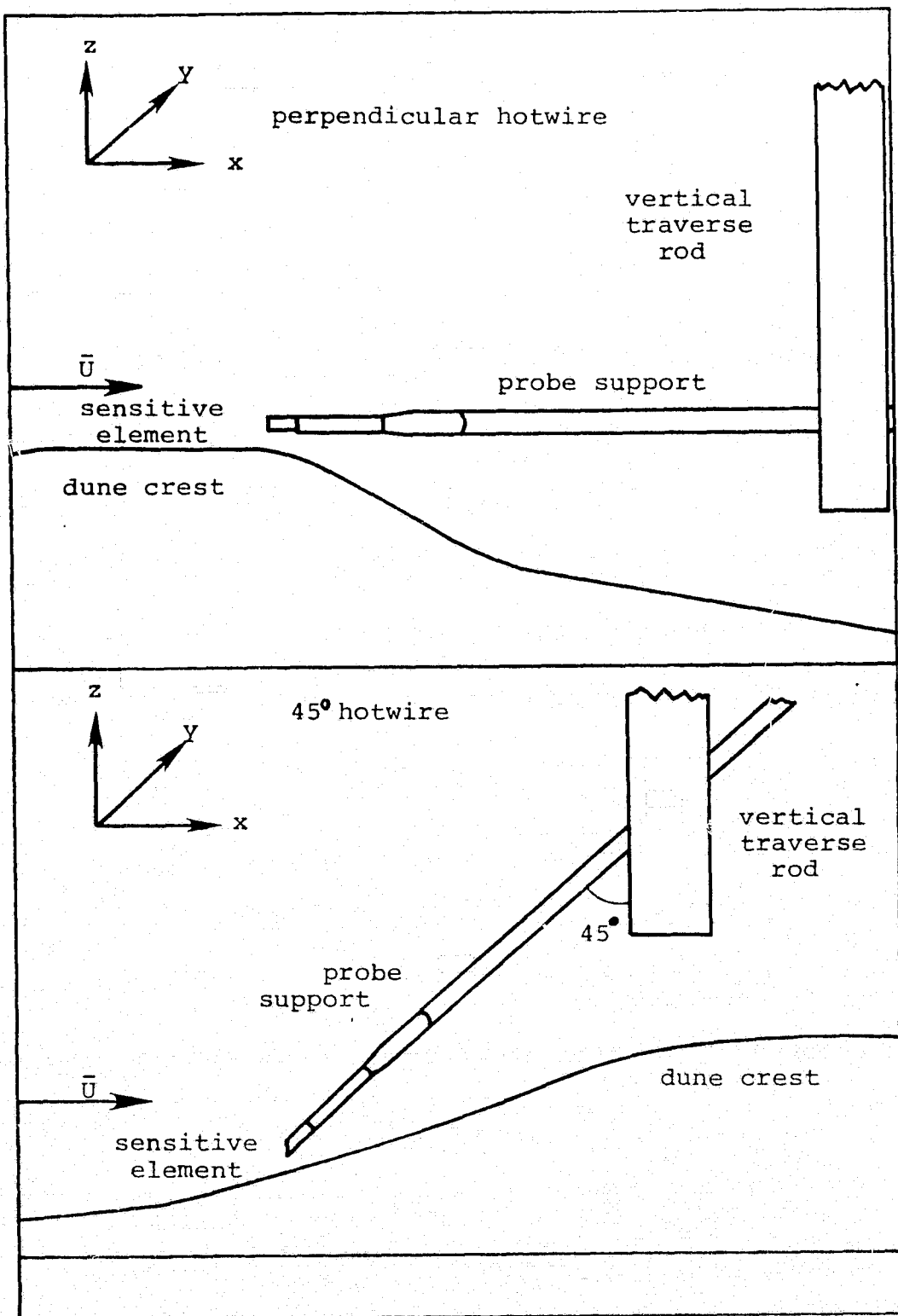


Figure 13: Perpendicular and 45° Hotwires

probe allows accessibility to the upwind slopes of the dune that would otherwise be inaccessible due to interference from the probe support.

A system was devised whereby hotwires could be calibrated and the wind tunnel drift monitored without the insertion of a pitot tube. A manometer, having resolution of 0.05 mm of water, is connected by rubber hoses to static pressure ports upwind of the contraction and at an x-location on the test section, close to the dune models. The manometer reads the difference in static pressure, from which the mean wind velocity can be calculated using Bernoulli's equation. With logarithmic and turbulence grids removed, the "reference" manometer reads the same values for wind speed as a pitot tube positioned at  $z_r$ . With grids and roughness elements inserted, the relationship between the velocities determined by the pitot tube and the reference manometer is linear.

For each profile measured, the tunnel drift was thus monitored and was restricted to 0.4% of the mean velocity at  $z_r$ .

### 3.3 The Use of Flow Visualization as a Wind Direction Indicator

Hotwire measurements of profiles around dune models are sufficient to provide information about relative wind speeds at various spatial locations. However, only in one case is the hotwire used to directly indicate flow direction; this case will be discussed later in this section. In all other cases, the technique of flow visualization is employed to determine directional trends.

Several methods of flow visualization were investigated; the method of tufting proved to be the most successful. Thin strips of tissue paper, the "tufts," are glued at one end to the models being studied, attached in such a way as to have no initial directional bias. When the wind blows on the models, the tufts align themselves with wind direction, thus indicating streamlines on the dunes. Photographs are taken of the models at different exposure times to determine both "instantaneous" and "averaged" wind trends. A sample of tuft photography for barchan #1 is shown in Figure 14; 14(a) shows an instantaneous tuft alignment with an exposure time of 1/2 second and 14(b), taken at an exposure of 2 seconds, illustrates the average wind flow. It is from photographs of the averaged cases that streamline maps of the flow over the dune are drawn.

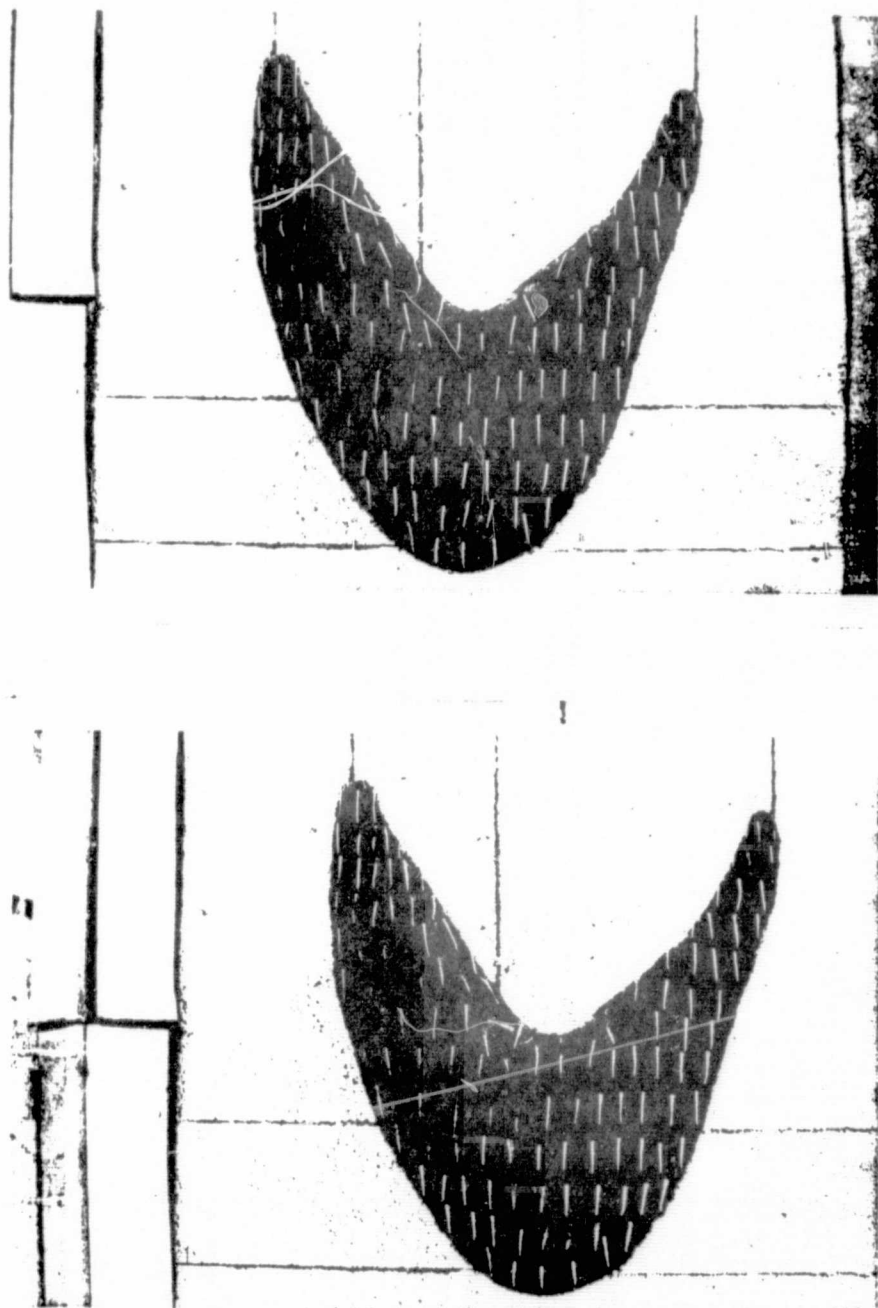


Figure 14: Tuft Flow Visualization Photographs of Barchan #1

At points near the base of the dune on the windward side, the tufts normally remain in one position, not always indicative of flow direction, because the wind at those points is not strong enough to move the tufts effectively. Clearly, for these points another method for finding wind direction is needed. It is in such a case that the hotwire is used as a direction indicator. The hotwire has an angular cosine sensitivity to the flow and may be rotated to find flow direction [27]. A 45° hotwire does not need to be rotated; it may be inserted into a stationary probe support in two different orientations: the first at an angle of 45° with respect to the x-axis in the positive y direction; the second at an angle of 45° in the negative y direction (Cf. Figure 15). Using the equation:

$$\tan \theta' = \frac{E_2 - E_1}{E_2 + E_1} \quad 3.3.1$$

where  $E_1$  and  $E_2$  are voltages (corresponding to velocity magnitudes) recorded at the two orientations, it is easy to compute the resultant angle,  $\theta'$ , at which the wind is blowing with respect to the x-axis. The angles thus calculated contribute to the streamline maps of the model dunes. In the next chapter, the resulting streamline maps and their importance in computing dune migration will be explored.

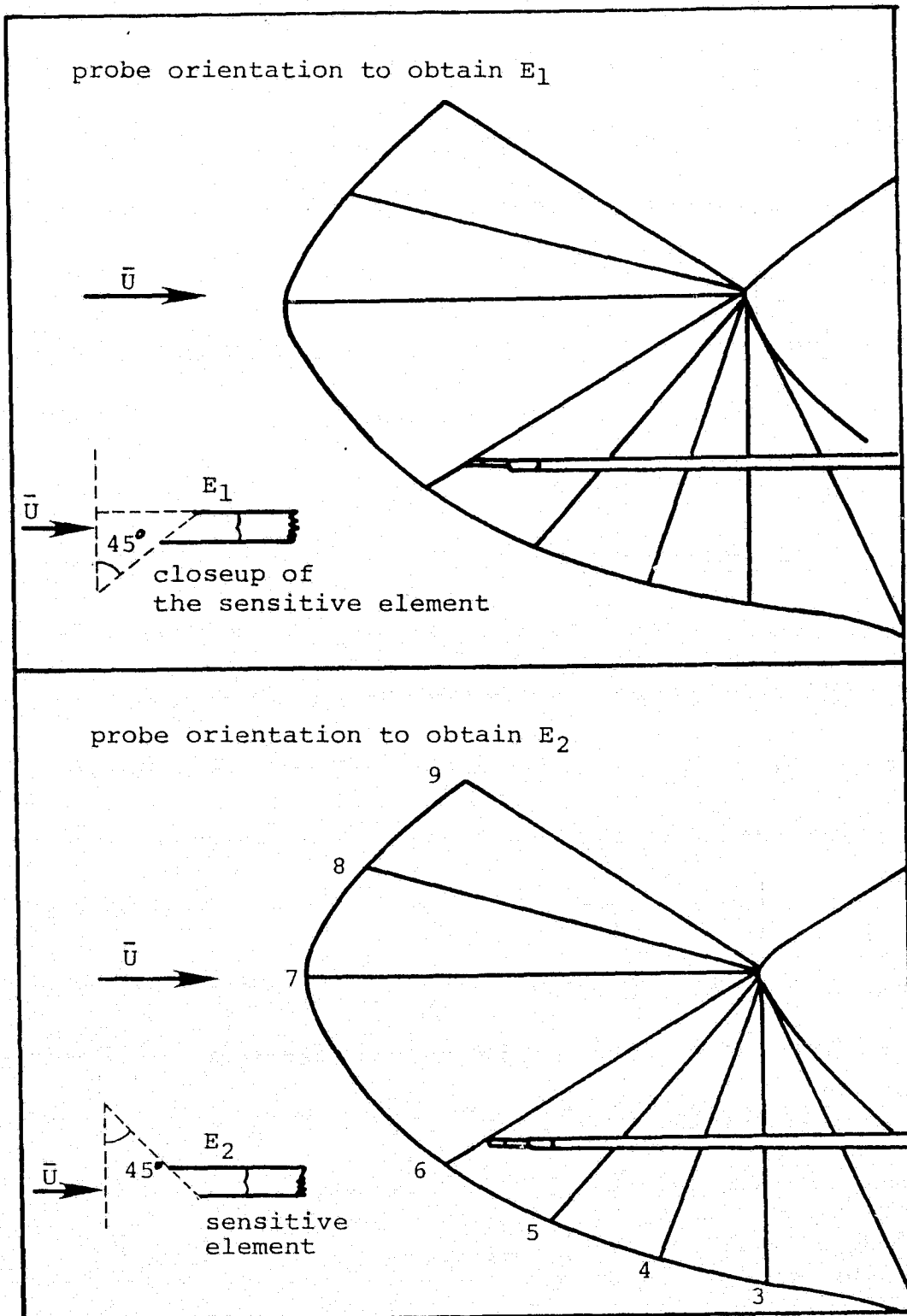


Figure 15: Orientations of 45° Hotwire

## Chapter 4

### EXPERIMENTAL RESULTS

#### 4.0 Velocity Profiles around a Barchan Sand Dune

In order to determine local friction velocities which are needed for the analysis of the sediment budget of a barchan dune, it was found necessary to measure an extensive set of velocity profiles. Hotwire measurements of  $\bar{U}$  were made up to heights far greater than was necessary to determine  $u_*$  values; one of the additional purposes of the measurements is to determine flow patterns of the wind above the saltation layer of the dune. Profile measurements provide the answers to basic questions about the interaction between the mean wind and the barchan.

From a study of these velocity profiles, it is possible to determine certain flow trends; for example: the height at which the flow resumes a logarithmic profile undisturbed by the dune is approximately equal to six times the maximum dune height. A region of reverse flow in the lee of the dune crest is detectable with a hotwire. Changing the speed of the mean velocity of the wind has no effect on the velocity profiles other than a scaling effect; if the mean wind speed is doubled, for example, each of the velocities in the profiles is also doubled, to within 4% accuracy.

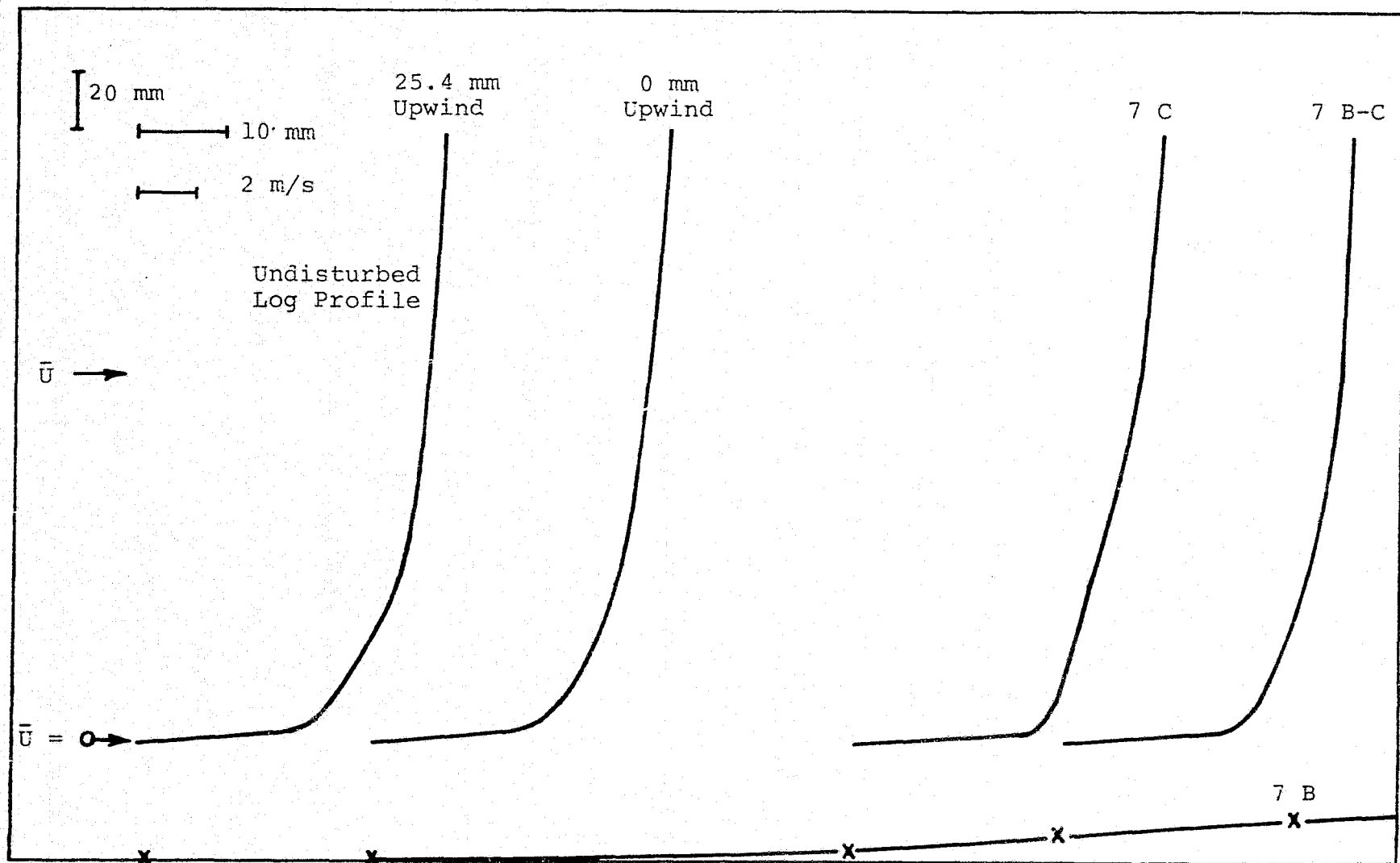
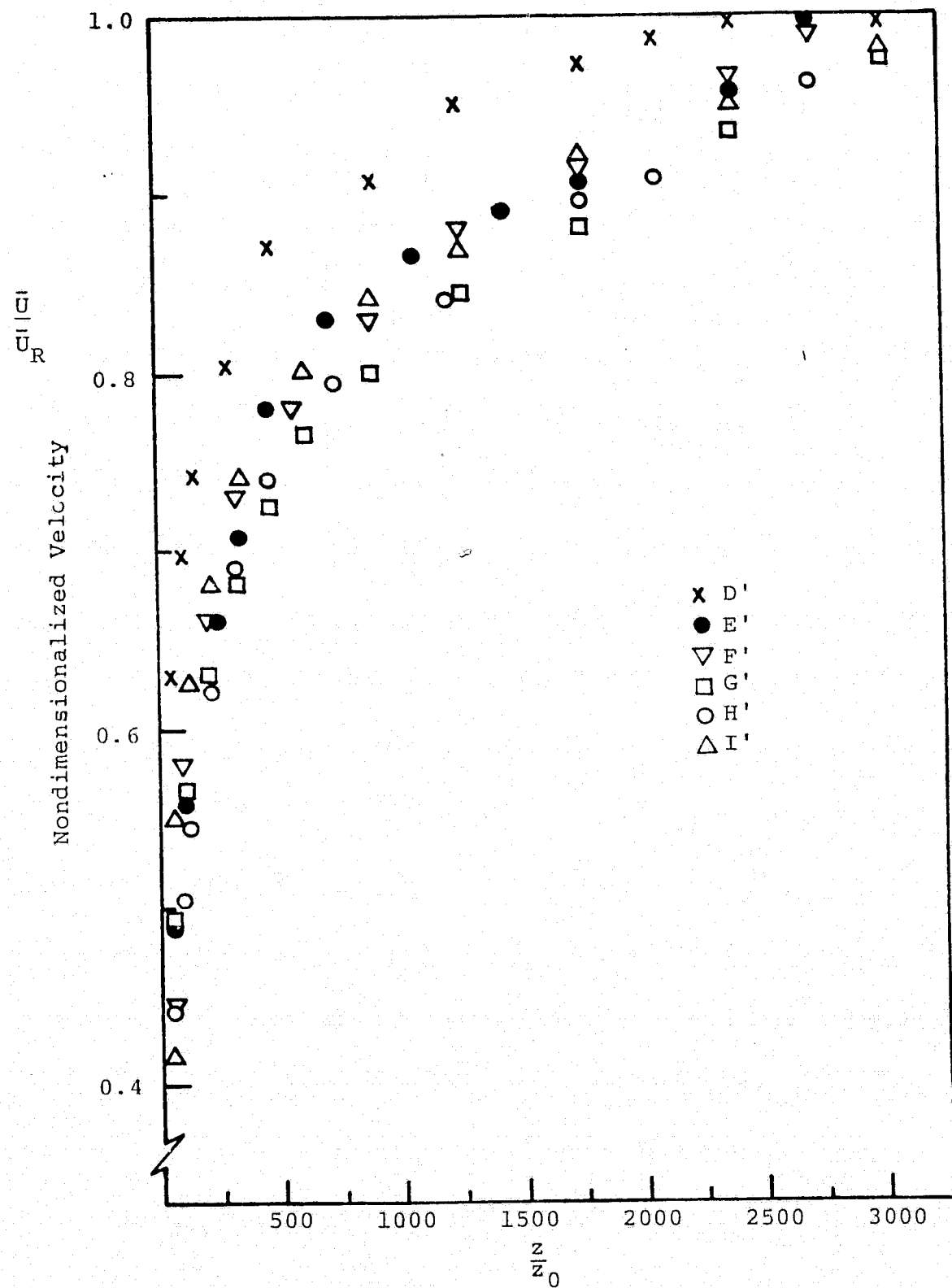


Figure 17(a); Velocity Profiles Along Line 7 For Barchan #1



Height above Tunnel Floor (Nondimensionalized)

Figure 16: Velocity Profiles in the Lee of Barchan #1  
(See Figure 12 for locations of positions D' - I')

at a decreasing rate as the crest is approached, so that the profiles converge and become logarithmic at  $z = 160$  mm. Profile  $\alpha$ , in the lee of the dune, possesses a very low velocity for  $z \leq 10$  mm which actually decreases initially as  $z = 10$  mm is approached, then greatly increases to converge with the other profiles. The hotwire is not able to adequately interpret reverse flows, so it can only meaningfully be used at  $\alpha$  to determine the location of this "dead" zone in the lee of the crest, and not its characteristics. The dead zone is seen to be approximately 10 mm high and extends no more than about 90 mm downwind from  $\alpha$ .

Similarly, profiles measured on the wings of the dune model were studied to determine flow trends. For convenience, the wing on which lines 8-13 are drawn is called wing A and wing B is the wing on which lines 1-6 lie. On wing A, between height contours 6.3 mm and 9.5 mm [Cf. Figure 18], the wind attains its greatest near-surface ( $\xi' = 2.54$  mm) velocity at line 11, which is exactly perpendicular to the oncoming mean wind. Thus, the flow experiences an acceleration along that location of the wing and a deceleration as the sheltered portion of the wing (lines 12 and 13) is approached. Along the crestline of wing A, the velocity at  $\xi' = 2.54$  mm decreases downstream; this is to be expected, because the height  $z$  of the crestline decreases downstream also. A relatively high velocity (at  $\xi' = 2.54$  mm)

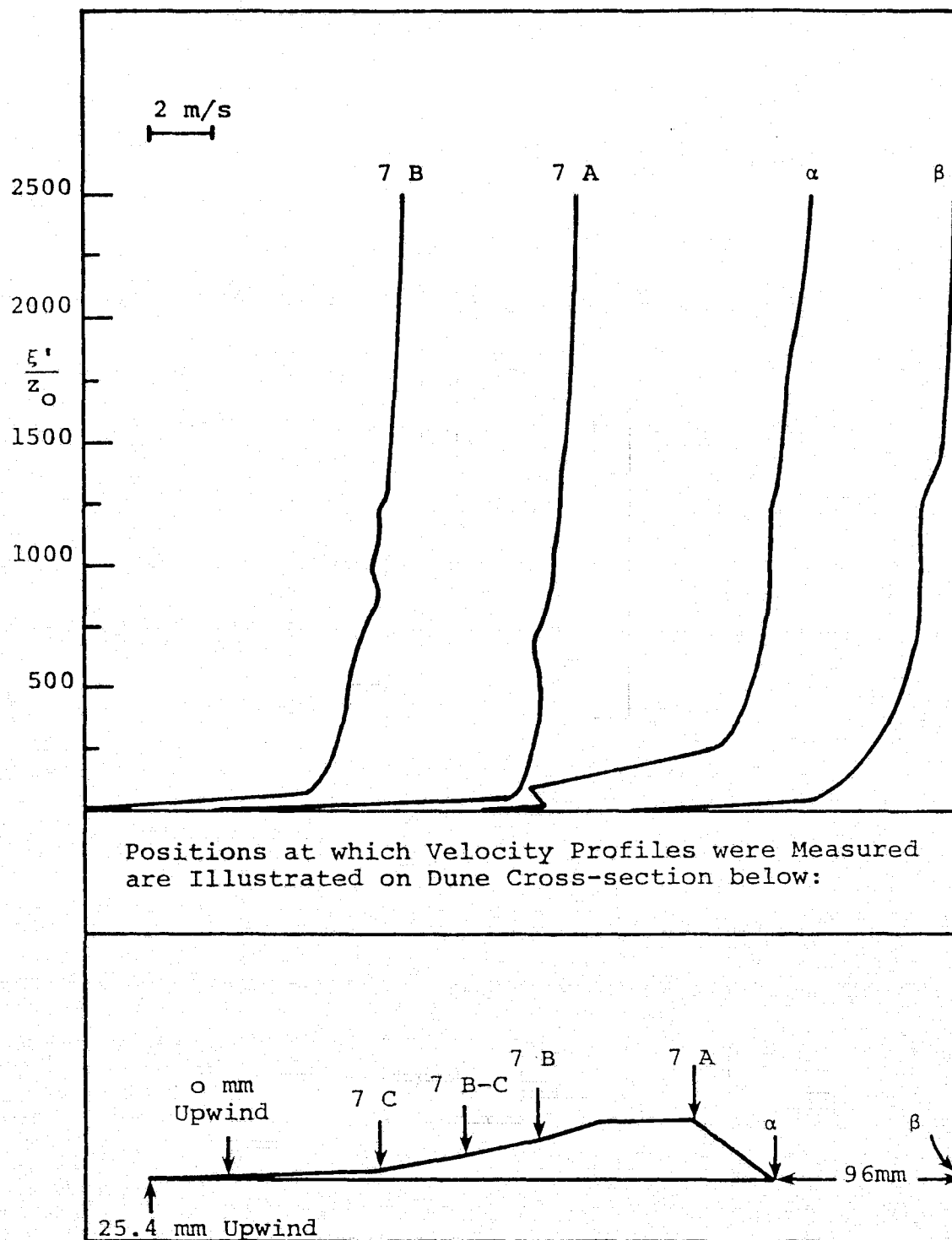


Figure 17(b): Velocity Profiles Along Line 7 for Barchan #1

occurs at the wing tip, indicating a convergence of flow at that point [Cf. Figure 26]. For all cases except at the tip, the velocity increases from the lower contours of the dune to the crestline. All of the profiles measured on wing A converge at  $z \approx 60$  mm (scales to a field height  $z \approx 19$  m, approximately three times the maximum dune height) with each other. In general the profiles at the crest converge with each other at  $z = 20$  to  $z = 25$  mm. On both wings, between contours 1.27 and 1.59, the local wind is deflected slightly away from the wing tips and towards the center of the crest.

Analyzing profiles of wing B, one notices that between contours 0.63 and 0.95, the maximum near-surface velocity occurs at line 4, which is not perpendicular to the oncoming wind, rather than at line 3, which is. The probable explanation for this is that at line 3 the wing is indented slightly, which has the effect of protecting it from the wind; at line 2, the wind accelerates again, where the wing protrudes outward. The profiles on wing B converge at  $z \approx 0.1$  m, with the crestal profiles being the last to converge with the lower ones; the crestal profiles converge with each other, however, at  $z \approx 30$  mm.

A set of velocity profiles was measured, for a tunnel reference speed  $\bar{U}_R = 10$  m/s in the lee of the dune at six locations laterally positioned at a distance 210 mm down-

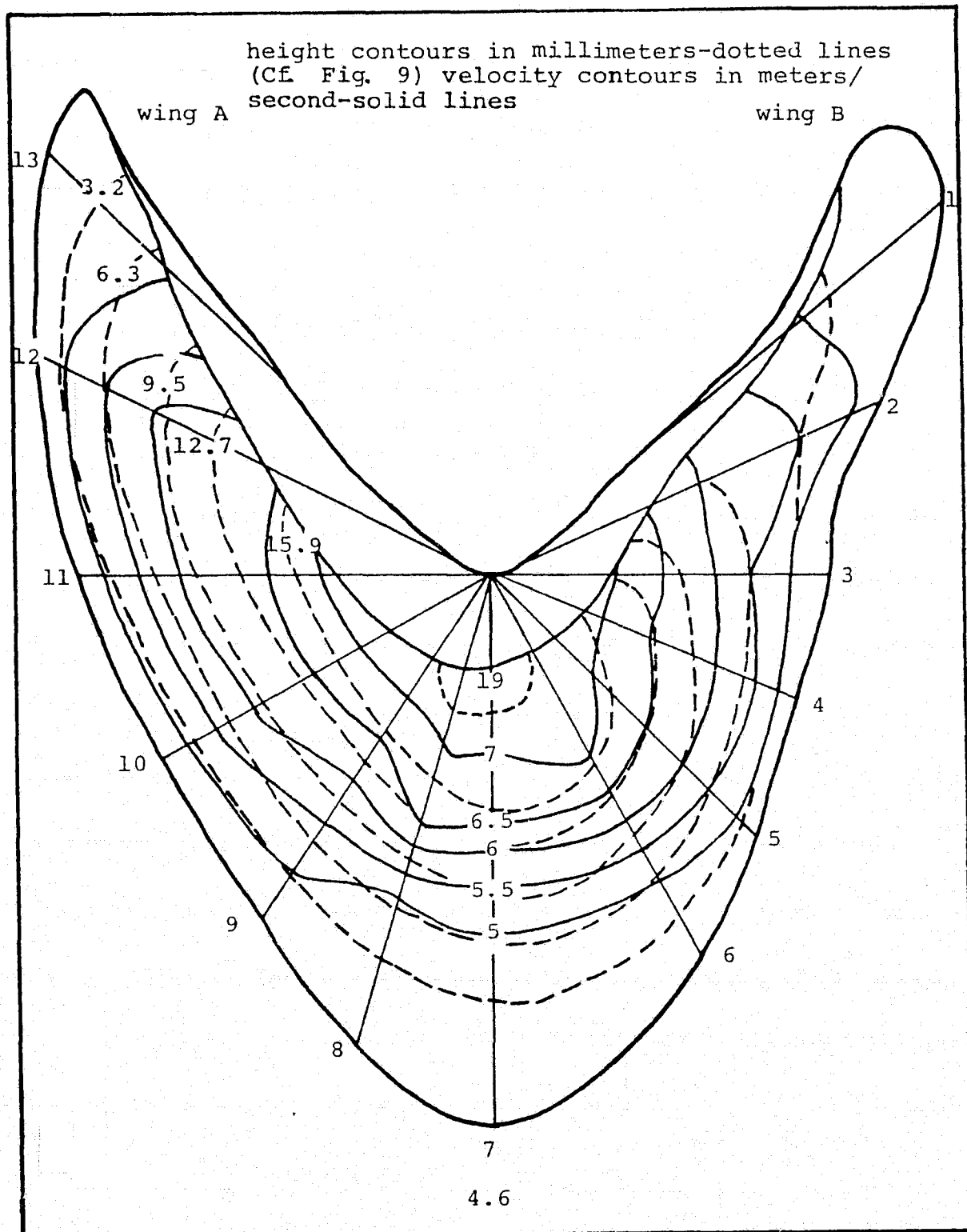


Figure 18: Velocities at  $\xi' = 2.54$  mm. Superimposed on Height Contours for Barchan #1

occurs at the wing tip, indicating a convergence of flow at that point [Cf. Figure 26]. For all cases except at the tip, the velocity increases from the lower contours of the dune to the crestline. All of the profiles measured on wing A converge at  $z \approx 60$  mm (scales to a field height  $z \approx 19$  m, approximately three times the maximum dune height) with each other. In general, the profiles at the crest converge with each other at  $z = 20$  to  $z = 25$  mm. On both wings, between contours 12.7 and 15.9, the local wind is deflected slightly away from the wing tips and towards the center of the crest.

Analyzing the profiles of wing B, one notices that between contours 6.3 and 9.5 the maximum near-surface velocity occurs at line 4, which is not perpendicular to the oncoming wind, rather than at line 3, which is. The probable explanation for this is that at line 3 the wing is indented slightly, which has the effect of protecting it from the wind; at line 2, the wind accelerates again, where the wing protrudes outward. The profiles on wing B converge at  $z \approx 0.1$  m, with the crestal profiles being the last to converge with the lower ones; the crestal profiles converge with each other, however, at  $z \approx 30$  mm.

A set of velocity profiles was measured, for a tunnel reference speed  $\bar{U}_R = 10$  m/s in the lee of the dune at six locations laterally positioned at a distance 210 mm down-

stream with respect to  $\alpha$  [Cf. Figure 16]. Profiles E', F', G' and H' converge and begin to become logarithmic at  $z = 95$  mm; profiles D' and I' do not converge until a height  $z = 210$  mm is attained. Velocities recorded for the profiles at a height  $z = 2.54$  mm are studied in order to determine a flow pattern for the dune.

A rough pattern of "streamlines" is drawn from the measurements [Cf. Figure 19]; the pattern resulting at  $z = 2.54$  mm coincides closely with Allen's streamlines in the lee of a barchan dune [19].

The effect on velocity profiles of changing  $\bar{U}_R$ , the tunnel reference speed, was investigated. Velocity profiles were measured at key points on the dune (7A, 13 crest and 2 crest) and at a point 10 cm upwind of the dune at tunnel speeds of 5, 6, 7, 8 and 10 m/s. A scaling factor by which velocity profiles could be normalized to a single reference speed (10 m/s) was sought. The value of predictability of profiles for different oncoming wind speeds is that it can be used to cut down considerably on the number of measurements necessary to determine flow around the barchan dune.

The most obvious method of determining scaling factors was investigated first and proved to be fruitful. Each point in the velocity profile is multiplied by a scaling factor equal to  $\bar{U}_R/\bar{U}_x$  where  $\bar{U}_R = 10$  m/s and  $\bar{U}_x$  is the

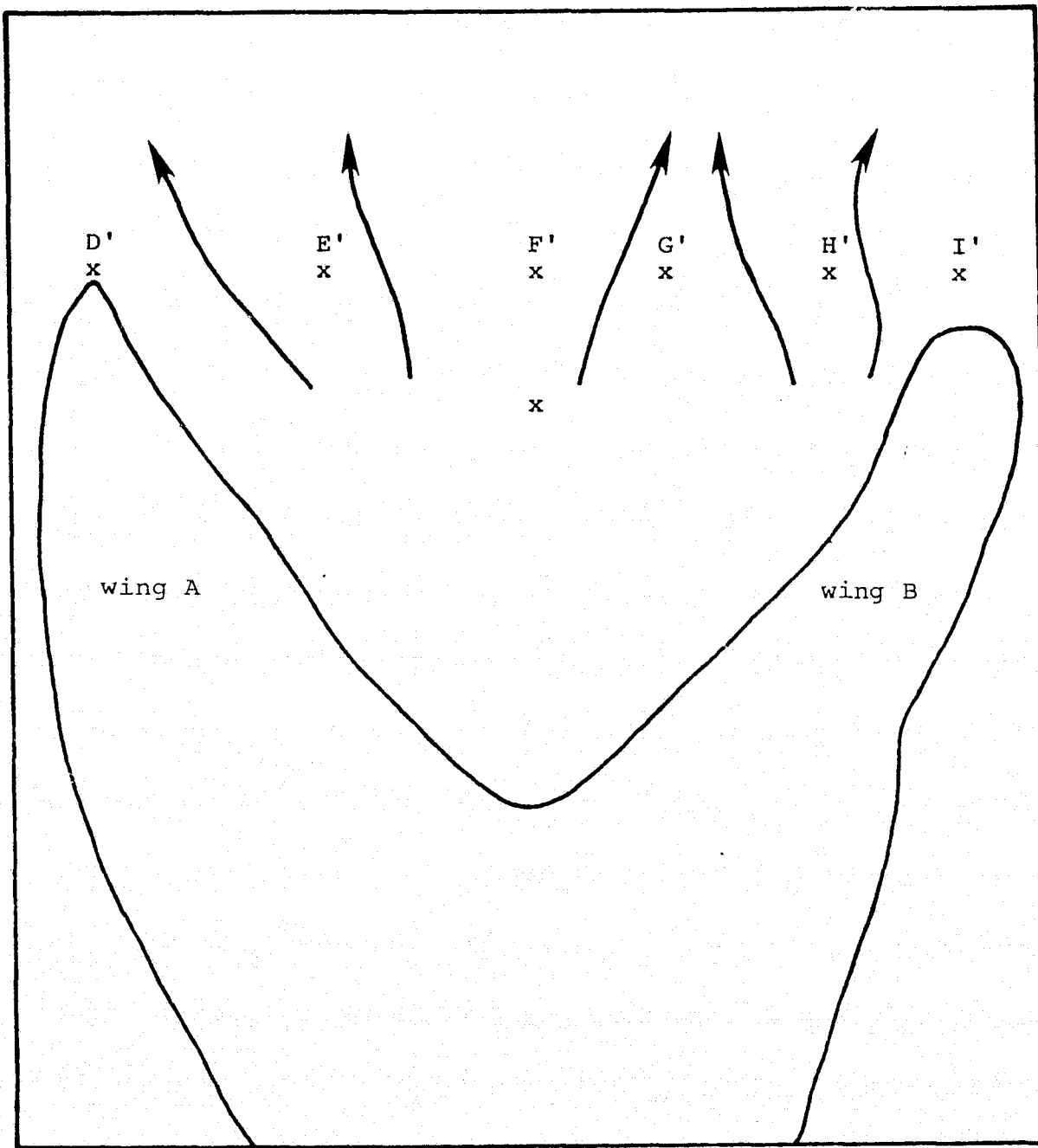


Figure 19: Qualitative Directional Wind Pattern derived from Velocity Profiles in the Lee of Barchan #1

tunnel reference speed for the profile. The scaled profile is plotted on a graph with a profile measured at the same location for  $\bar{U}_R = 10$  m/s. The degree of collapse may thus be evaluated, or the velocities may be individually compared to find a percentage difference between them.

Figure 20 shows sample velocity profiles measured at 7A at tunnel speeds of 5 and 10 m/s; the profiles are nondimensionalized by dividing by the appropriate reference speed. The two profiles coincide closely with an average error of 1.3%; most of the difference occurs close to the dune's surface. The other profiles yielded similar results with an overall average percentage difference of 4%. Later in this section, the source and magnitude of the errors will be presented. It will be shown that the average percentage error in determining velocity profiles is about 3.8%, so an error of 4% may be said to lie within experimental error. In conclusion, the velocity profiles may be scaled in the manner described above to obtain a representation of the profiles at some desired wind velocity. Reynold's number effects are thus found to be negligible for wind tunnel speeds used in the experiment.

An experiment was performed to determine the extent to which the logarithmic boundary layer artificially produced in the tunnel affects velocity profiles around the

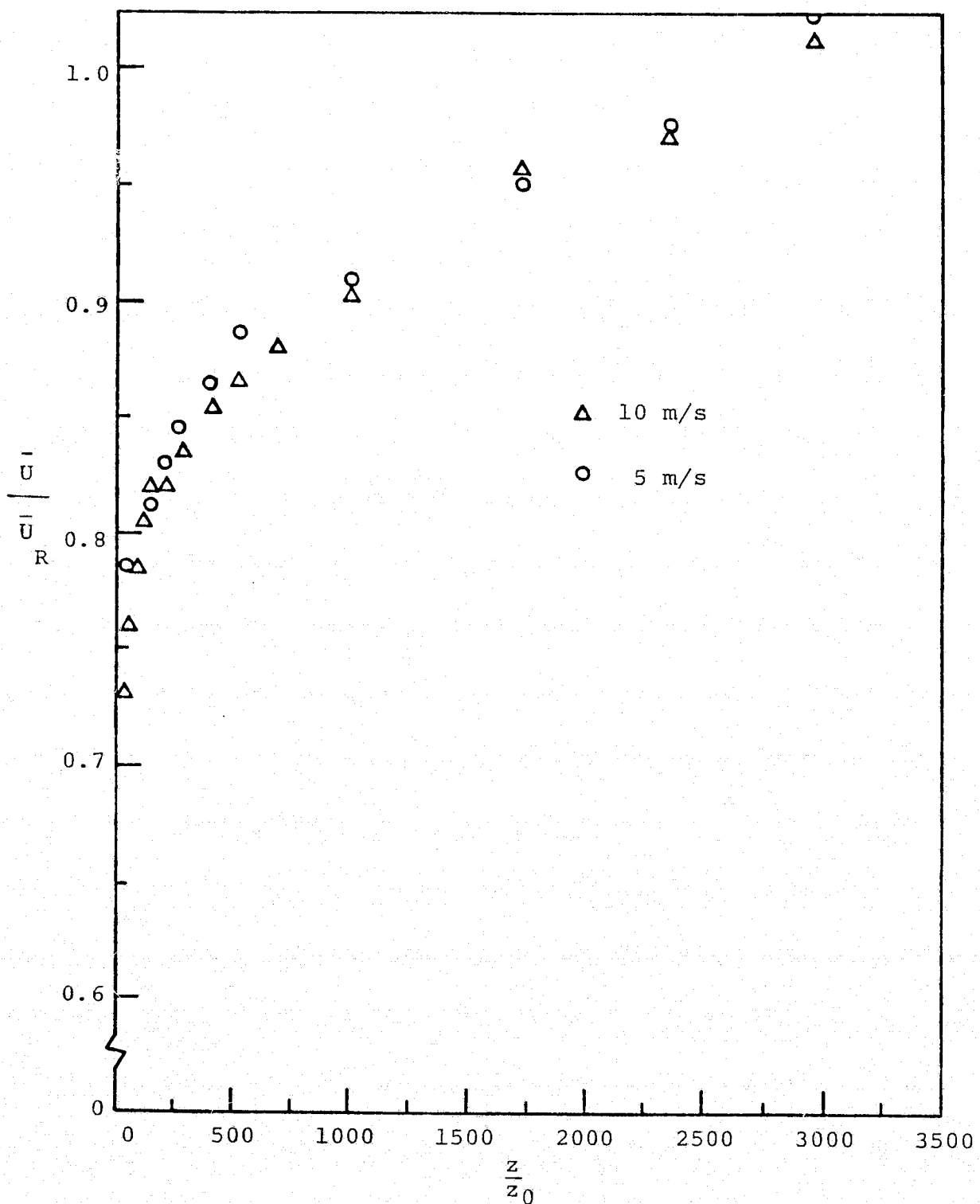


Figure 20: Scaled Velocity Profiles at 5 and 10 m/s

dune model. Profiles were measured at certain key locations on the dune with the turbulence and logarithmic grids and the roughness element removed. Removing the grids and roughness element resulted in the formation of a naturally grown boundary layer in the wind tunnel very close to the tunnel floor; for convenience, this flow shall be called "uniform," since the flow above the boundary layer is uniform, up to the heights at which measurements were made. The profiles thus determined were compared to profiles measured at the same positions in the logarithmic boundary layer. Figure 21 is a sample comparison. It is evident that the two profiles are dissimilar. At the point closest to the surface of the dune, where the dune affects the flow to the greatest extent, the percentage difference between the two velocities is 5.7%. The difference increases to a maximum of 12.11% at  $z/z_0 = 1000$ , then drops as the profiles converge at  $z/z_0 = 2750$ , where the logarithmic velocity at that height becomes equal to the free-stream velocity. The two profiles separate again as  $z$  increases beyond  $z/z_0 = 2750$ . From the results above and similar results obtained from other profiles, it is established that a simulated boundary layer is necessary if an accurate representation of wind flow over a barchan dune in the atmosphere is to be obtained, provided that the atmospheric boundary layer is really logarithmic.

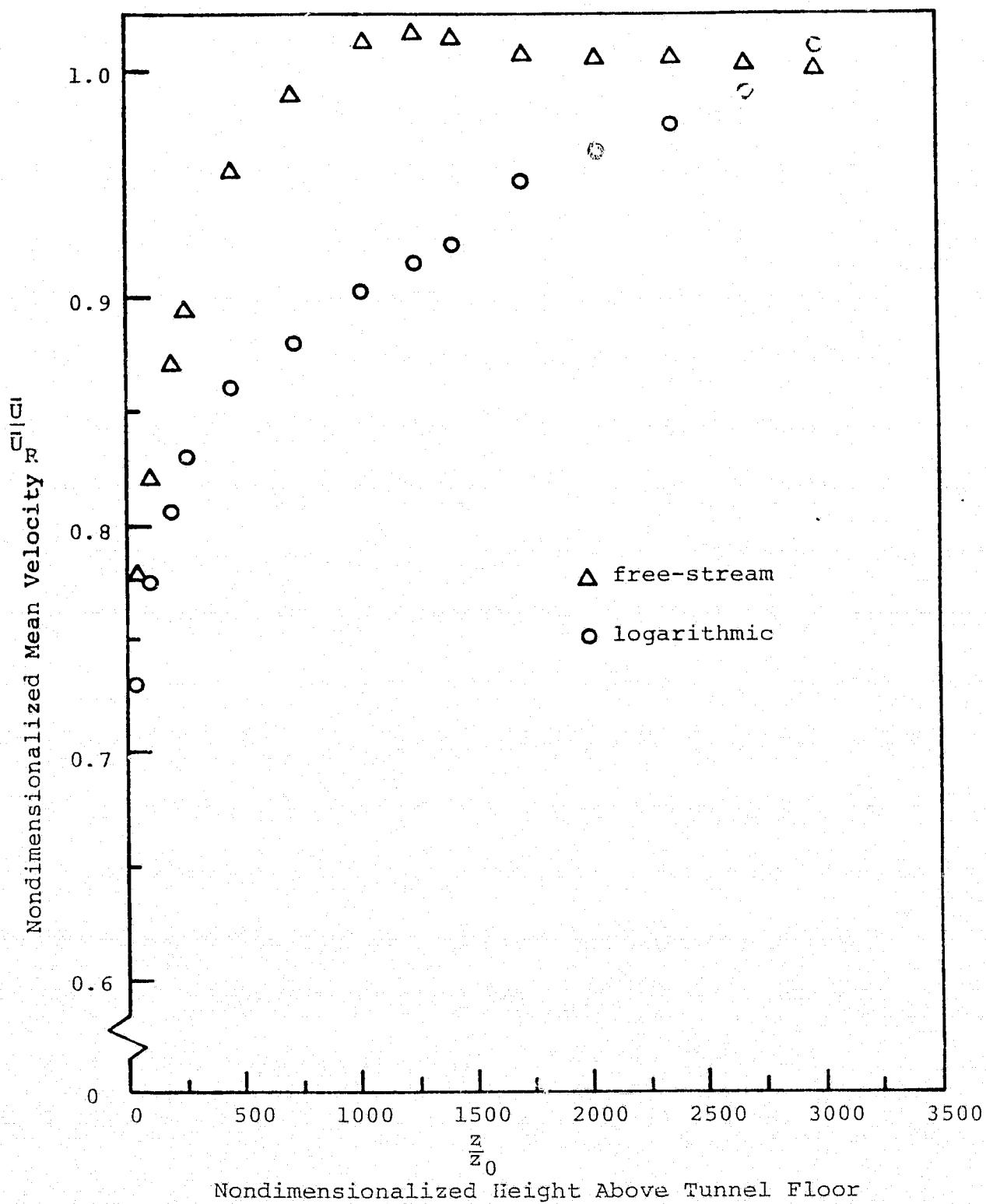


Figure 21: Comparison Between Free-Stream and Logarithmic Velocity Profiles

A brief investigation was made into the effects on velocity profiles of changing the angle of the oncoming wind with respect to the dune. The dune was rotated (horizontally, about the axis at point  $\alpha$ ), through angles of  $-30^\circ$  to  $30^\circ$  with respect to the mean wind, at  $10^\circ$  intervals. Profiles were determined, for  $\bar{U}_R = 10$  m/s, at positions 13 crest, 7A and 2 crest. Figures 22, 23, 24 and 25 show the resulting velocity profiles for positions 2 crest and 13 crest.

At an angle of  $30^\circ$ , wing A and, thus, 13 crest, is exposed more directly to the oncoming wind and wing B is partially sheltered. The "sheltering" effect can be observed in Figures 22-25. Velocities near the surface of 13 crest are highest when the mean wind impinges at  $30^\circ$  and become progressively lower as the wind is rotated to an angle of  $-30^\circ$ . The opposite effect, as expected, occurs for wing B. The velocity profiles converge at  $z/z_0 = 3000$ . The effect of changing the angle of attack of the wind on the velocity profiles and on the sediment budget of the barchan is one that demands more research.

The predominant source of error in the measurement of mean velocity profiles above the model occur in the positioning of the hotwire at locations close to the dune's surface. The distance between the sensitive element of the probe and the desired location on the model was measured with a vernier accurate to 0.01 cm, but some

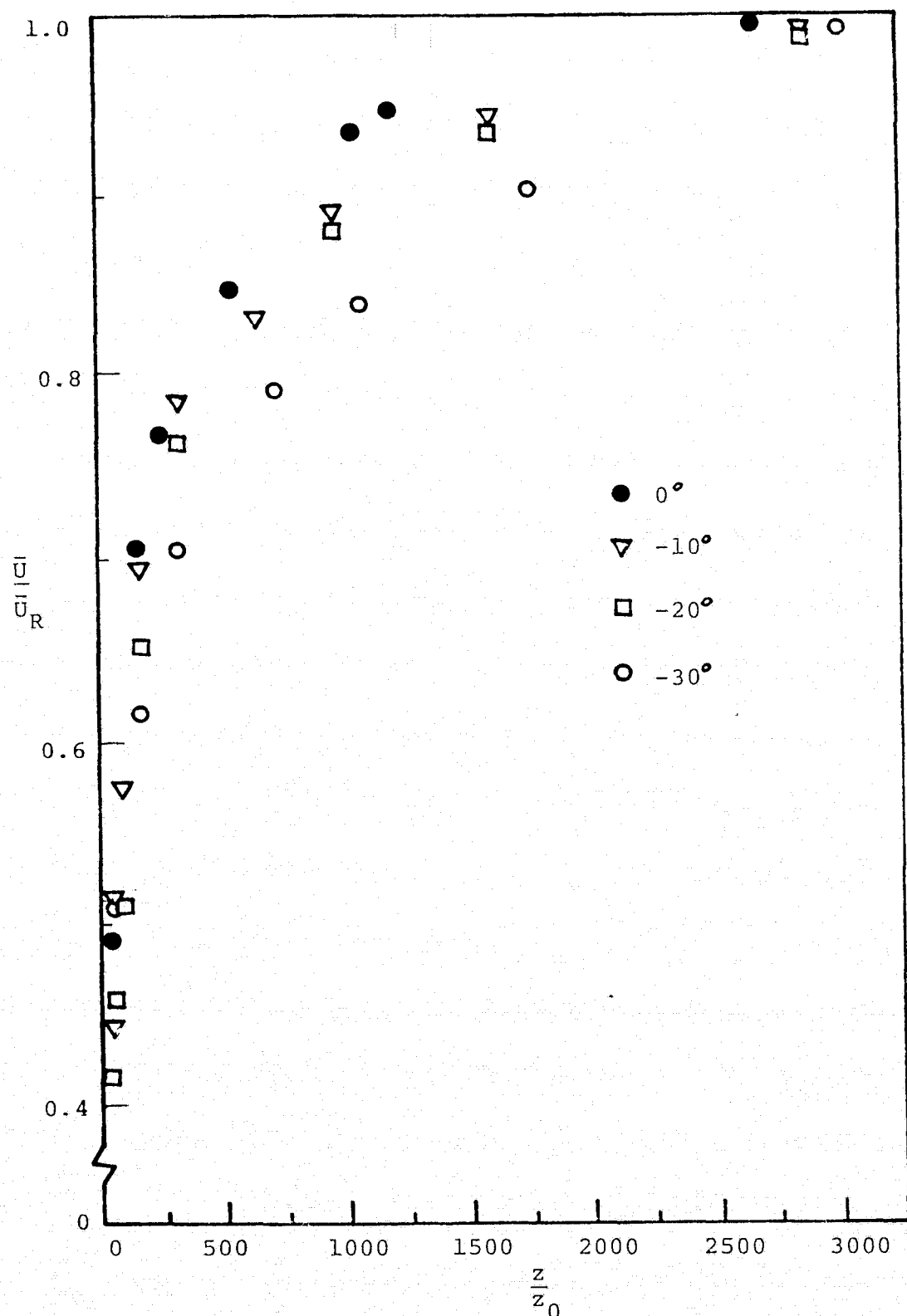


Figure 22: Velocity Profiles at 13 Crest (13 A') with Change of Wind Angle ( $0^\circ$  to  $-30^\circ$ )

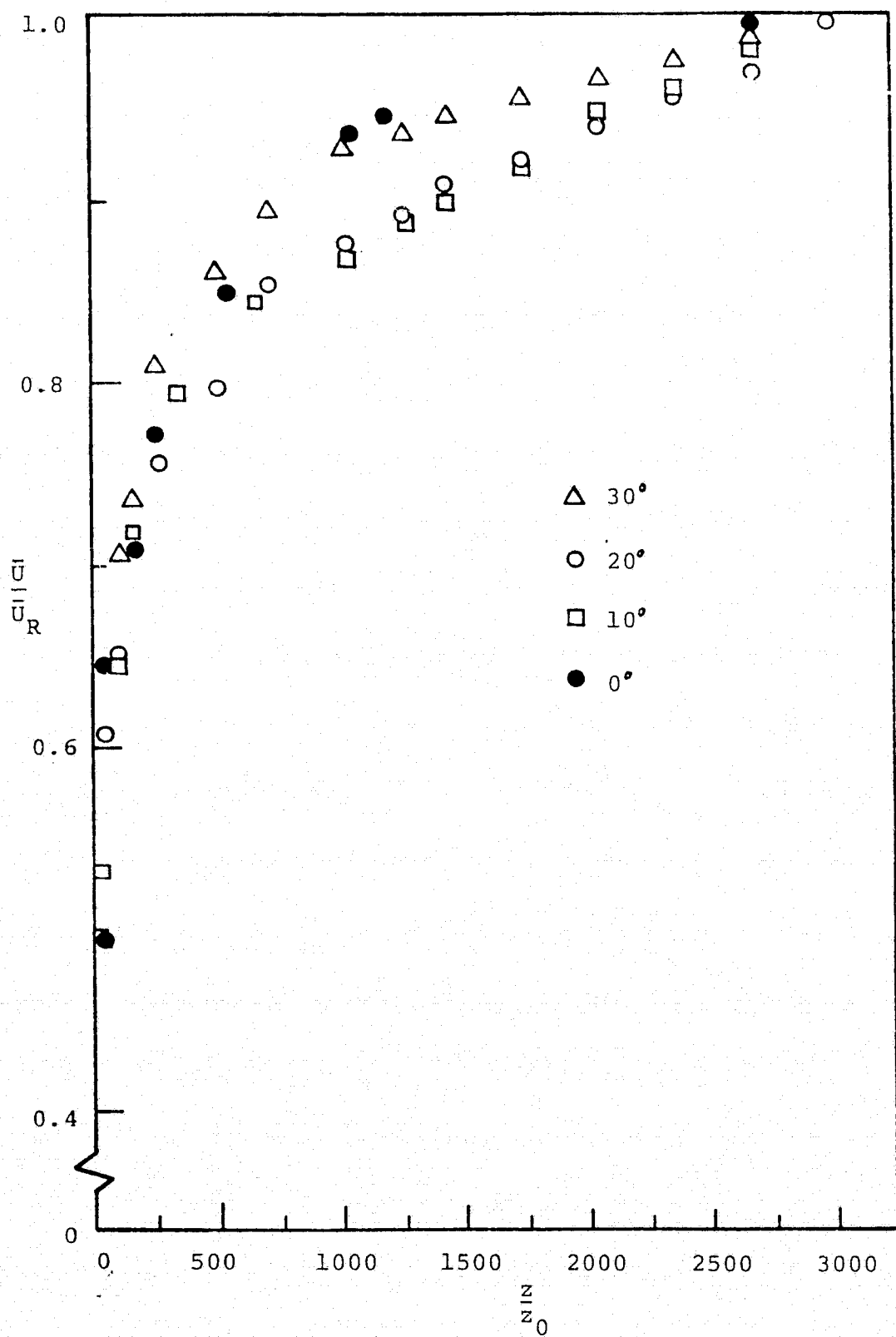


Figure 23: Velocity Profiles at 13 Crest (13 A') with Change of Wind Angle ( $0^\circ$  to  $30^\circ$ )

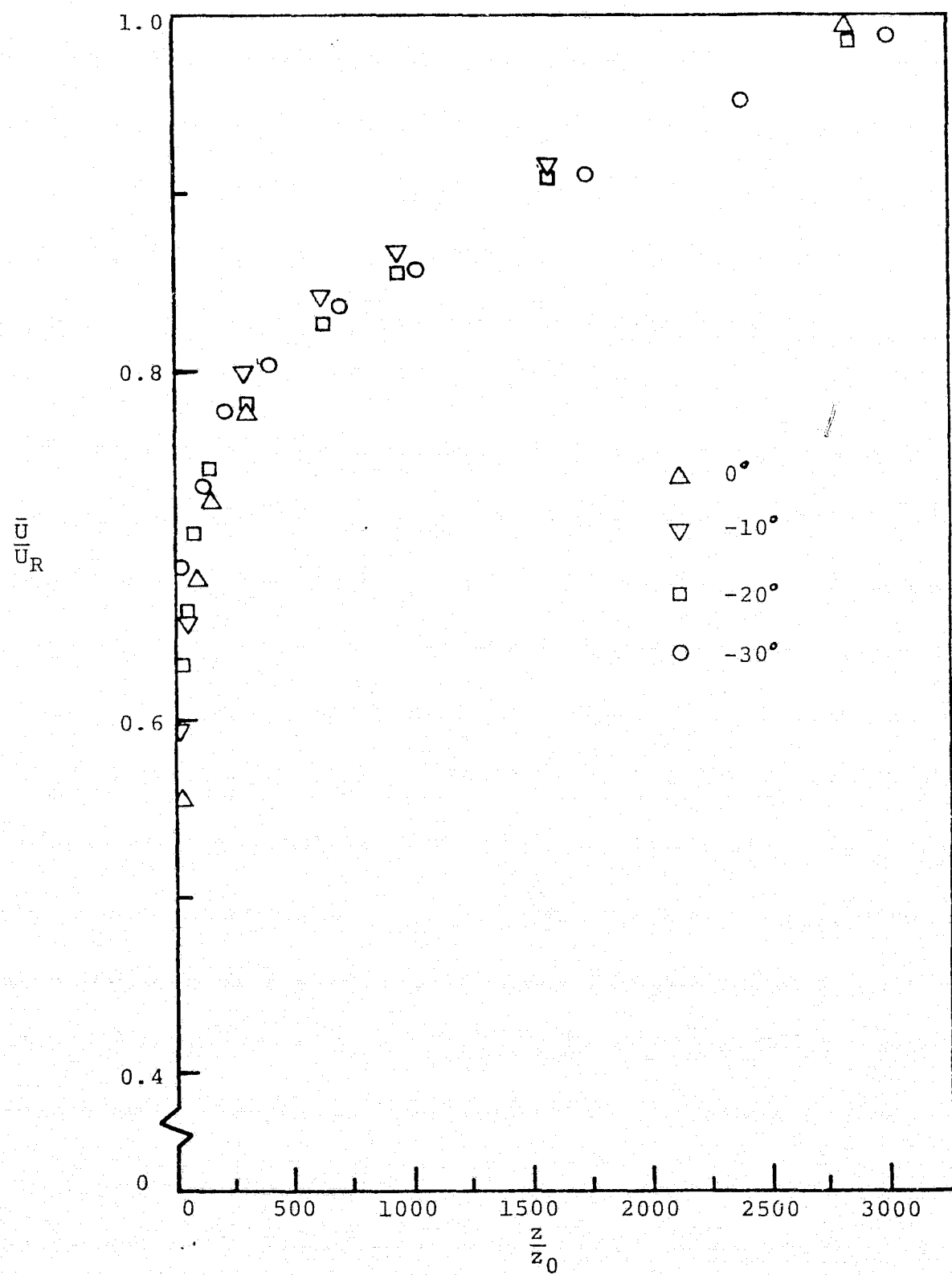


Figure 24: Velocity Profiles at 2 Crest ( 2A' ) with Change of Wind Angle (  $0^\circ$  to  $-30^\circ$  )

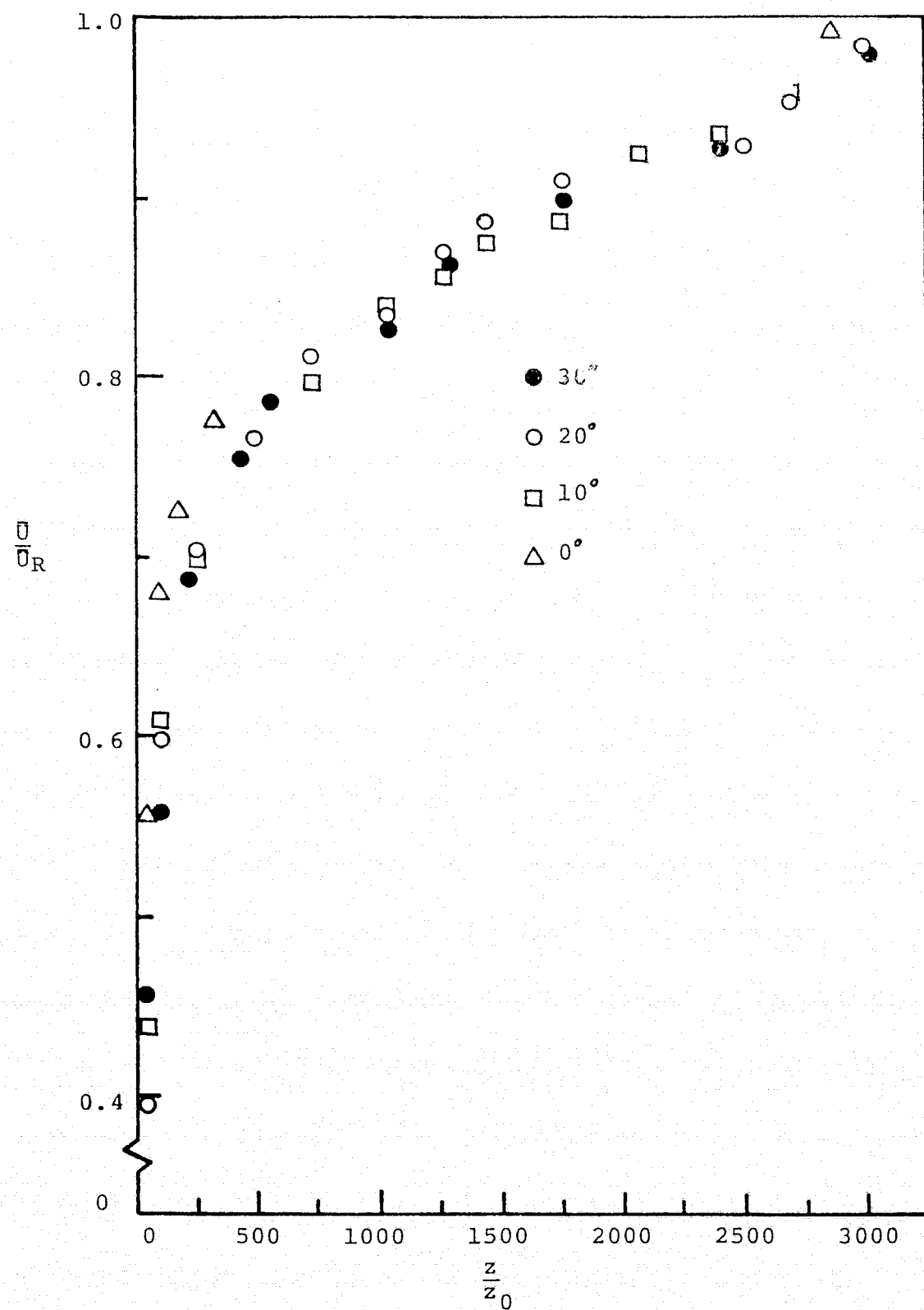


Figure 25: Velocity Profiles at 2 Crest (  $2A'$  ) with Change of Wind Angle (  $0^\circ$  to  $30^\circ$  )

difficulty was experienced, due to the extreme delicacy of the probe, in getting the vernier close enough to the sensitive element to make a reliable reading. Also, under the influence of the oncoming wind, the sensitive element often moved slightly from its initial position, requiring an additional adjustment of the hotwire's height, which had to be estimated visually. Assuming a displacement of 1 mm for the hotwire from the desired vertical location at each position, the average percentage of error for a complete velocity profile is 2.2%. (This error was calculated using equation 2.1.2 and varying  $z$  by 1 mm). The error from hotwire displacement varies from 15%, at  $\xi' = 2.54$  mm (where  $\xi'$  is the vertical distance) of the sensitive element from the surface where the profile is determined), to 0.1%, at  $\xi' = 230$  mm.

At locations close to the surface, particularly in the area of the crest and wings of the model, the turbulence intensities were quite high. The damping circuit on the voltmeter used to determine the mean velocity was sometimes not adequate to deal with turbulent fluctuations, and an estimate had to be made of the voltage, which on occasion fluctuated by as much as 2% of the mean velocity. Tunnel drift and hotwire calibration together accounted for about 0.2% error in all velocity profiles. Totaling percentages of the sources of error listed above, and

assigning an average value of 1.4% to turbulent fluctuations, the average error resulting from velocity profile measurements is equal to 3.8% of the mean velocity in the wind tunnel.

#### 4.1 Local Friction Velocities on the Barchan Dune

The method used for determining values for the local friction velocity,  $u_*$ , on the barchan dune is discussed in section 2.1. Equation 2.1.6 yields values of friction velocity as a function of the velocity at a height  $z = 2.54$  mm in the tunnel, equivalent to a height of 0.8 m in the desert. Using the  $C = 2.22$  in equation 2.1.6, friction velocity values are calculated for each location at which velocity profiles are determined on barchan #1. Figure 26 is a contour map of the local friction velocities drawn from a map of calculated  $u_*$  values.

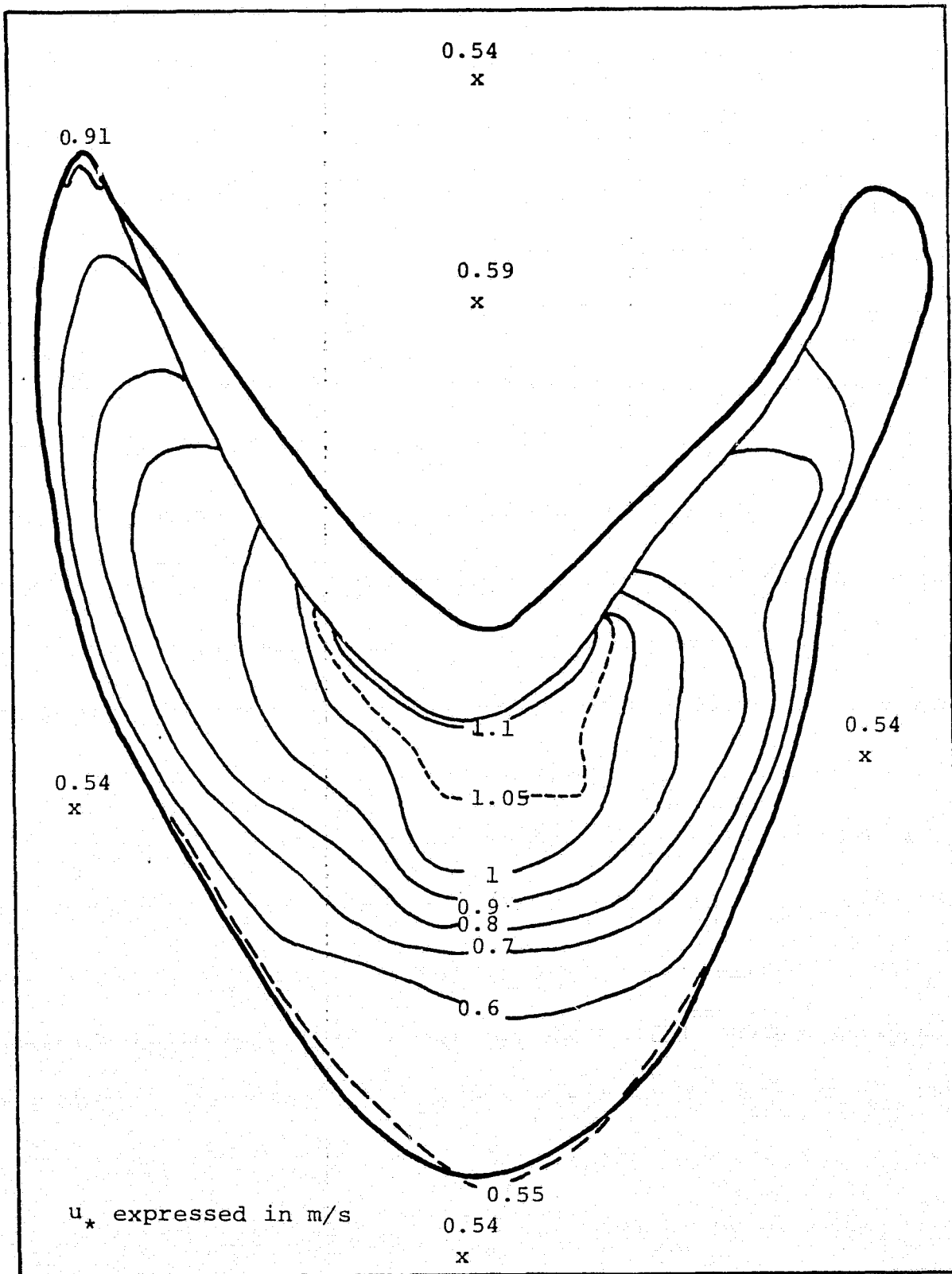


Figure 26: Contours of Measured  $u_*$  Values for Barchan #1

#### 4.2 Streamline Mapping of Barchan #1

In determining the sediment budget for barchan #1, it is necessary to construct accurate streamlines for the dune. The streamlines are subsequently divided into "cells" of equal length, and values for erosion or deposition of sand are computed for the center of each cell.

Three different methods are employed in determining streamlines for barchan #1. The first streamline map [Cf. Figure 27] was drawn from a combination of tuft photographs and directional measurements made at the base of the model with a 45° hotwire probe, using the method outlined in section 3.3. The tufts in the photographs are aligned with the local wind; streamlines may be interpolated between the tufts from points slightly upwind of the dune base to points on the crest. Local wind vectors determined with the hotwire at the dune's base are added to the tuft streamlines to form a complete streamline map of the model.

Measurements made in the field for barchan #1 provide the second method for determining local wind streamlines for the dune [1]. Stakes were implanted on the dune's surface and the directions of the scour marks resulting from wind action were measured using a compass. The "vectors" determined by the scour marks were measured for two different mean wind orientations, impinging from

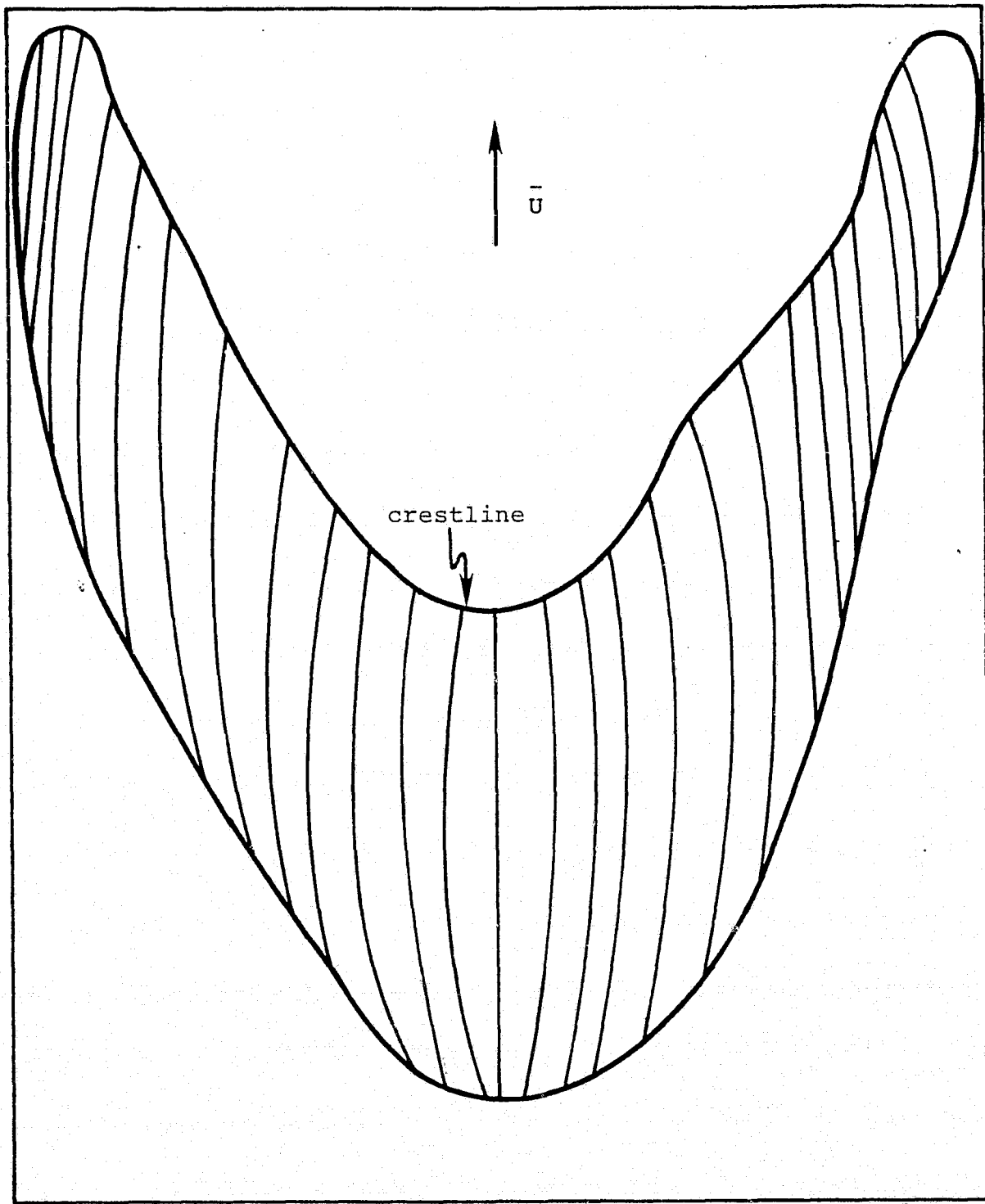


Figure 27: Streamline Map of Barchan #1 (From Tuft Photographs)

N73E and from S81E. The desired local wind vectors are for the case where the mean wind impinges from N82E (the orientation of the dune model in the wind tunnel), so a "weighted mean" value for local wind direction at a mean wind of N82E is calculated from values obtained in the field. Streamlines are drawn from the direction indicators thus derived in combination with vectors obtained in the wind tunnel with the hotwire at the dune's base. Figure 28 is a streamline map determined using the second method for finding local wind vectors.

The third method for determining "streamlines" for a barchan dune assures a local wind always perpendicular to local ripple marks. From reference 1, ripple strike measurements were made in the field for barchan #1 at the two wind orientations described in the previous paragraph, and vectors for the local wind direction for an impinging mean wind at N82E are interpolated from the two measured sets of vectors. Figure 29 is a map drawn from the local wind vectors derived from the ripple strike measurements; this map will be called a "ripple-line" map, because the lines on it are not streamlines. The sediment budget for the dune is calculated for the ripple-lines in Figure 29 in the same manner as for Figure 28: the paths determined by the ripple-lines are divided into cells of equal length, and erosion and deposition rates are de-

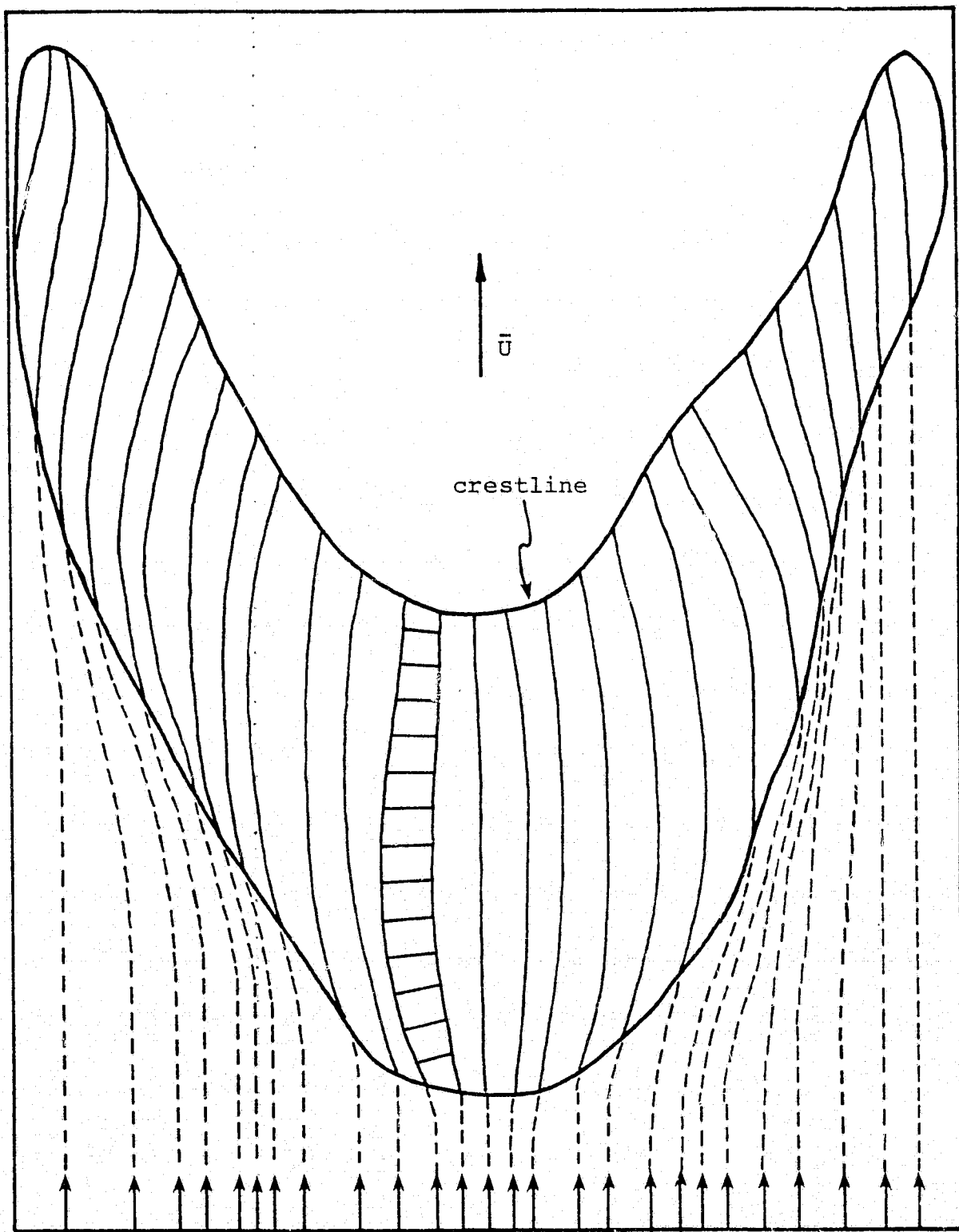


Figure 28: Streamline Map of Barchan #1 (From Field Measurements)

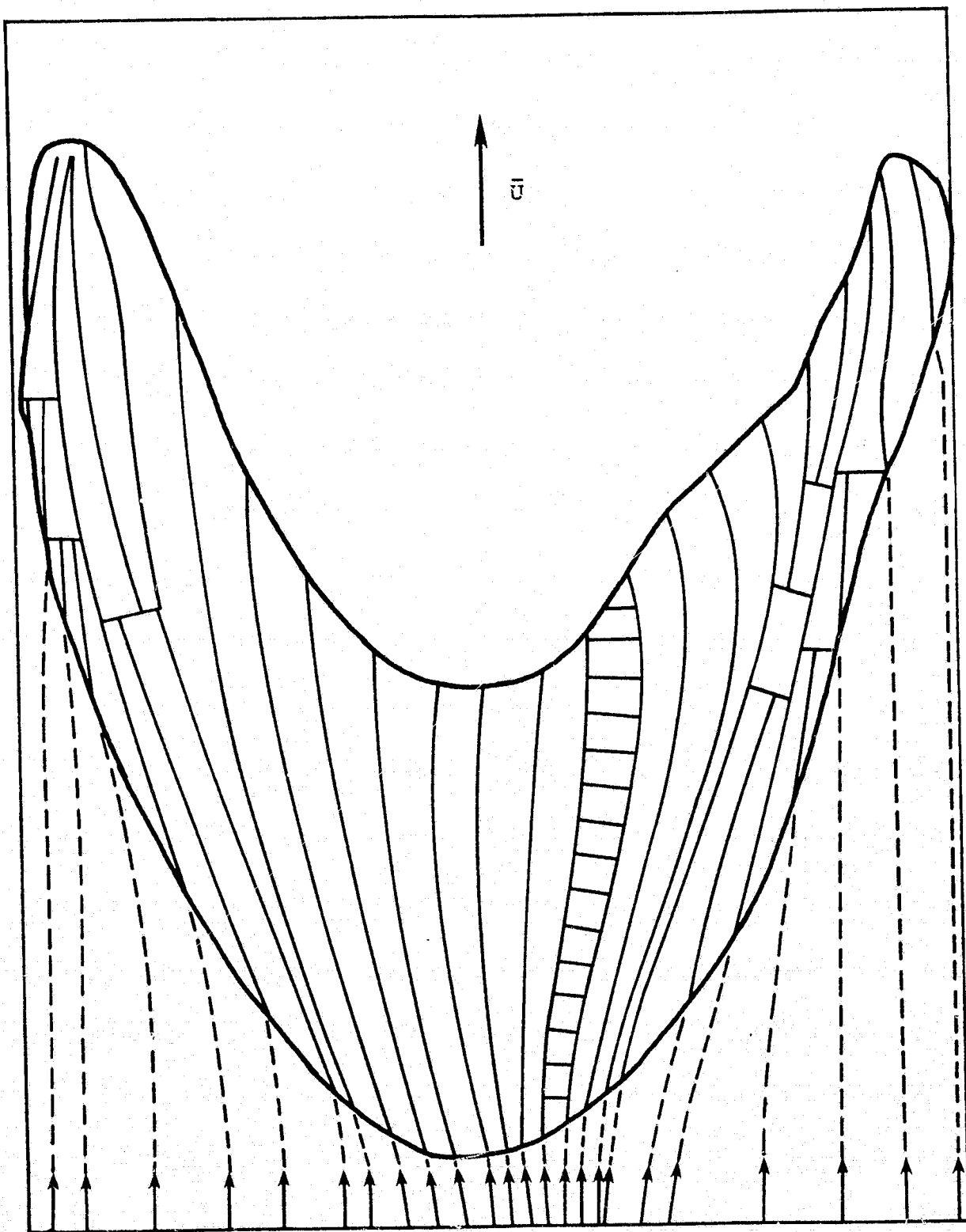


Figure 29: Ripple-line Map of Barchan #1

terminated for each cell. In Figure 29, certain ripple-lines on the wings branch off from others to form two separate ripple-lines. This occurs where the ripple lines are dense, indicating a strong convergence of local wind.

Patterns of erosion and deposition found in section 4.3 for the barchan dune, using the streamline and ripple line maps in Figures 28 and 29, will provide a comparison between the two "streamlining" methods. However, comparisons may also be made among all three maps by examining the figures. A comparison of the tuft streamlines and streamlines determined in Figure 28 from field measurements reveals many similarities between the two. Since the hotwire method described in section 3.3 was used for both maps to find directional trends at the dune's base, the streamlines in Figures 27 and 28 are initially identical. Both sets of streamlines diverge initially on the main section of the frontal slope upwind of the wings, then converge at the crest. Near the tip of wing A, both streamline maps indicate a strong convergence of flow toward the tip, rather than toward the crest; on wing B, both maps show a flow trend towards the crest for the local wind, rather than towards the wing tip.

The principle difference between the streamlines in Figures 27 and 28 occurs on the sections of the wings close to the main central portion of the dune. Figure 27

shows slightly greater convergence of local flow towards the wing tips than Figure 28 does (where "convergence," in this case, implies a bottleneck effect); the local wind in Figure 28 shows the greater flow tendency towards the crest. Because the two maps are so similar, only one, Figure 28, was selected for sediment budget analysis in section 4.3

Comparing Figures 27 and 28 to Figure 29, it is immediately evident that ripple-lines show greater convergence of flow towards the wings than the streamlines do. Streamlines following the measured local wind directions indicate a comparatively stronger flow towards the central crest area of the dune.

Flow lines for the maps in Figures 27, 28 and 29 are drawn by hand from photographs or drawings containing only the short, vector-like direction indicators determined in the field and wind tunnel. Some error must result from misjudgment in the interpolation of lines between the direction indicators. In an effort to minimize human error, the streamline maps were drawn independently several times by two different people, until the final copies were deemed suitable by both.

#### 4.3 Mapping the Sediment Budget for Barchan #1

The final stage of experimental results is a comparison of contour maps for the sediment budget of barchan #1. Contours obtained using various combinations of the equations outlined in section 2.2 and the results of the streamline and ripple-line maps in section 4.2 are compared with each other and with predicted and observed contours of erosion and deposition for the dune. All erosion and deposition contours are normalized with respect to the rate of forward motion of the dune.  $E_1$ , the erosion at a point 1 on the dune's surface, is equal to  $\Delta h / \Delta x$  where  $\Delta h$  is the decrease in the height of the surface at point 1 when the dune has migrated a distance  $\Delta x$ . Thus  $E$  and  $D$ , the deposition, are nondimensional;  $E$  is assigned negative values because  $h$  decreases during erosion, and  $D$  is assigned positive values since  $h$  increases with deposition.

Figures 30 and 31 are erosion and deposition contour maps drawn using the streamlines of Figure 28. Values for  $u_*$  used to obtain  $q$ , the sediment transport rate, are obtained from velocity profiles measured in the wind tunnel. The two sets of contours differ only by the slope factor used to determine  $q$ . Figure 30 is drawn using Bagnold's equation, as expressed by equation 2.2.1, for sand transport, neglecting the slope effects of the dune. Figure 31 results from using Bagnold's equation, as ex-

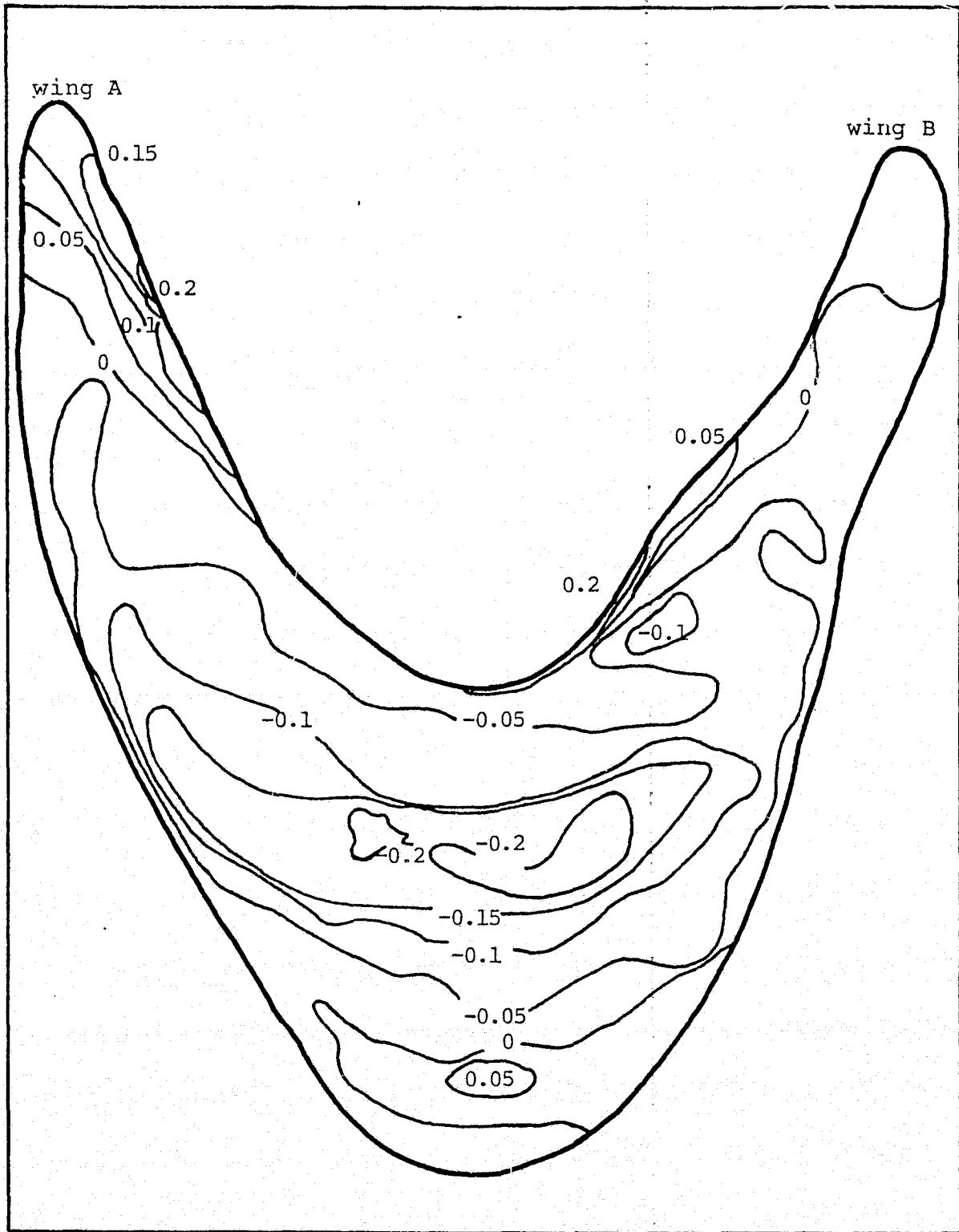


Figure 30: Erosion and Deposition Contours for Barchan #1  
( Neglecting Slope Effects, Using Streamlines from Local Wind ) The values represent dimensionless erosion and deposition, where negative values indicate erosion and positive values indicate deposition.

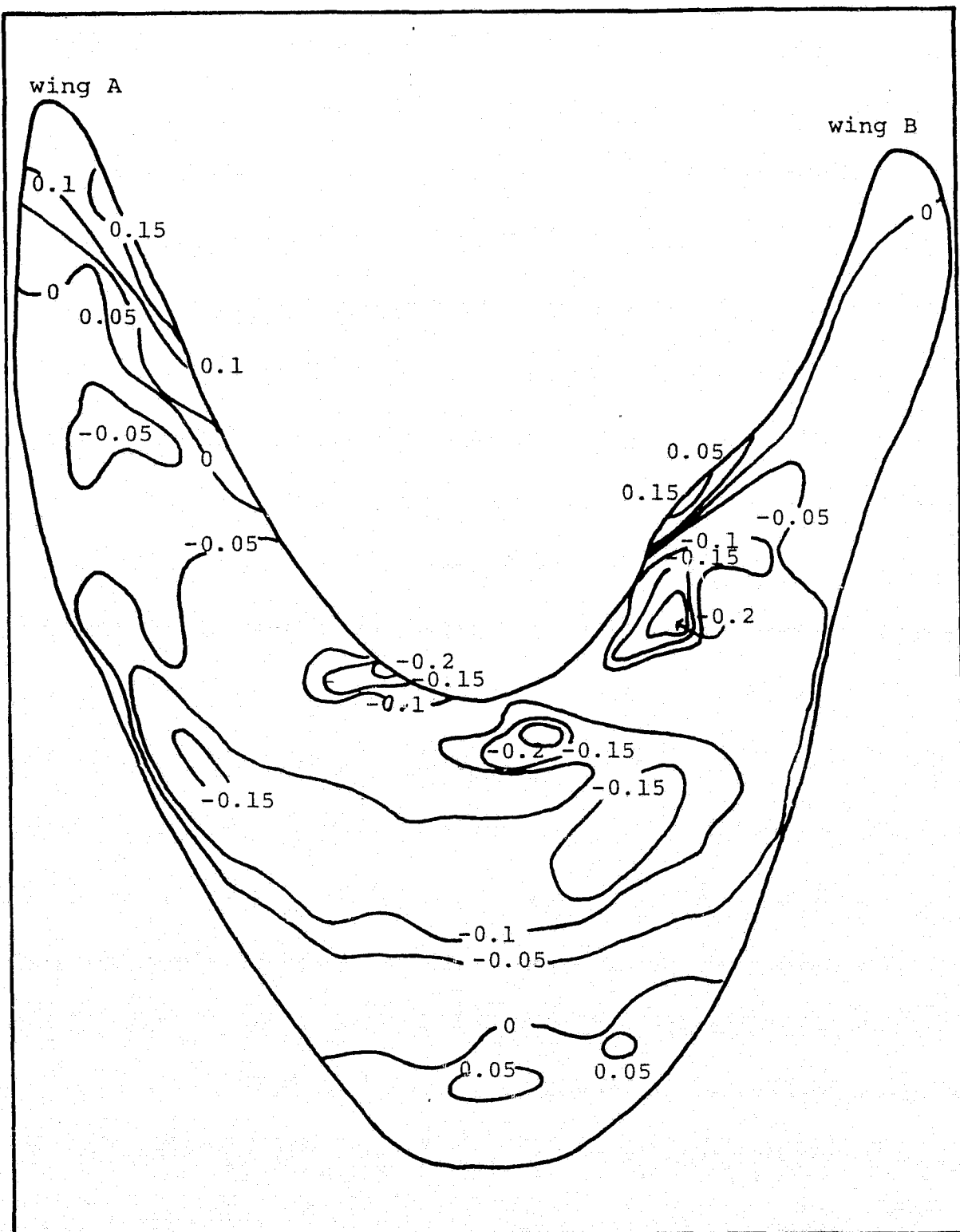


Figure 31: Erosion and Deposition Contours for Barchan #1  
( Including Slope Effects, Using Streamlines from  
Figure 12 )

pressed in equation 2.2.2. Contours for the tangent of the slope angle of the barchan, from reference 1, are given in Figure 32. From a visual comparison of the two figures, many similarities are evident. The contours on wing A in both maps are nearly identical. The portion of wing B near the central section of the dune in Figure 31 experiences less erosion than the corresponding location in Figure 30 does. In Figure 31, the main section of the dune experiences less erosion and the central crest section more erosion than in Figure 30. In general, the two maps show erosion in the central section of the dune, and on the wing areas closest to the central section. Deposition on the dune (as opposed to deposition in the lee of the crest) occurs on the wing tips.

Figure 33 is a contour map obtained from values of erosion and deposition found for the ripple-lines drawn from ripple marks in Figure 29. Again, Figure 33 is basically similar to Figures 30 and 31, where  $q$  is determined by the local wind. Erosion occurs on the main section of the dune and deposition takes place on the wing-tips and on a large section of the crest of wing A. In section 4.2, it was noted that the ripple-lines of Figure 29 indicate a strong convergence of flow along the wings; in Figure 33, deposition does occur on a greater portion of the wings than in the other two figures, but

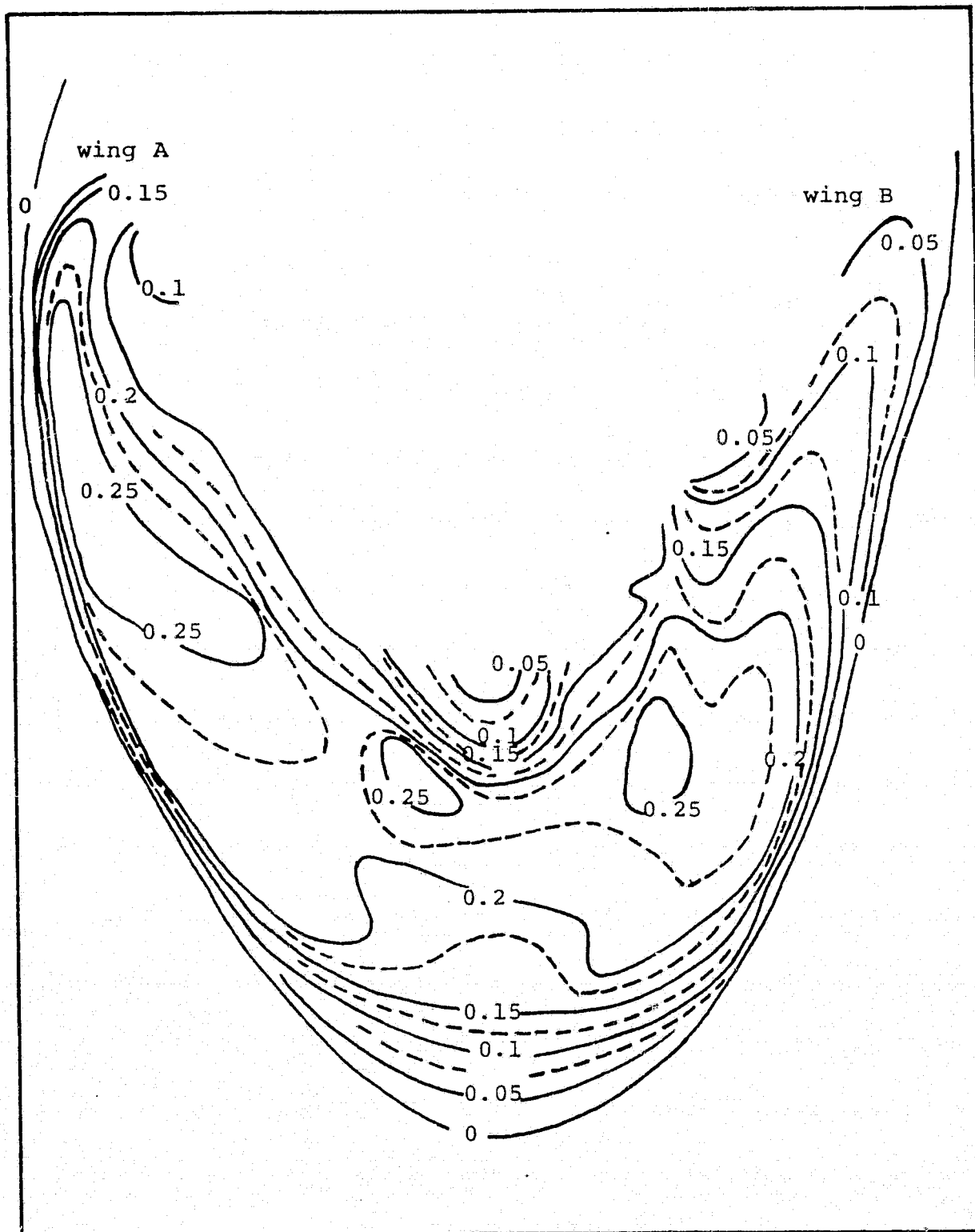


Figure 32: Map of  $\tan \theta$  Values for Barchan #1 ( Reference 1 )

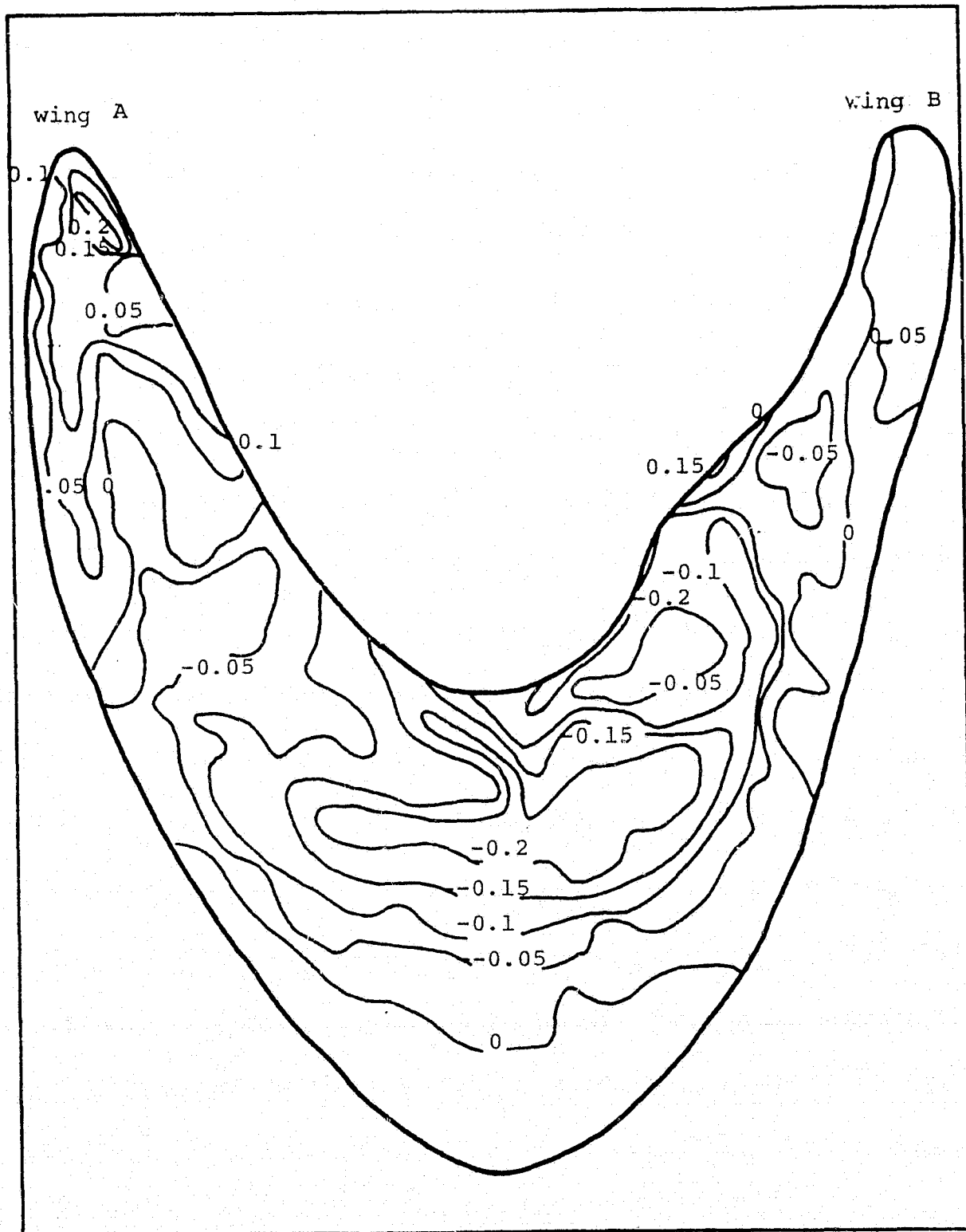


Figure 33: Erosion and Deposition Contours for Barchan #1  
(Including Slope Effects) Using Ripple-lines

there is relatively much less deposition on the crest of wing B. The erosion contours in Figure 33 on the main section shift towards the crest and show a higher erosion rate than either of the other sets of contours do.

Figure 34, from reference 1, shows sediment budget contours for the dune drawn from measurements made of stake exposure and burial over a two week period. The pattern of erosion on the dune's central section differs slightly from all the other cases discussed so far, in that the area where the greatest amount of erosion occurs is closer to the crest than in the other cases. There is more erosion on the tip of wing B and more deposition on the crest of wing A than in the other figures, but the erosion on wing A is similar in extent and location to that found in Figures 30 and 31.

Figure 35, from reference 1, is a map of the predicted erosion and deposition contours for barchan #1, if dune equilibrium is preserved [Cf. Appendix A]. Comparing the contours in Figures 30, 31, 33 and 34 with the predicted contours, it is evident that the sediment budget calculated for streamlines following the local wind bears the greatest resemblance to the predicted sediment budget. Erosion rates on the central portion of the dune are similar to those found for Figures 31 and 34. On wing B, the deposition on the crest for the predicted case is greater than for

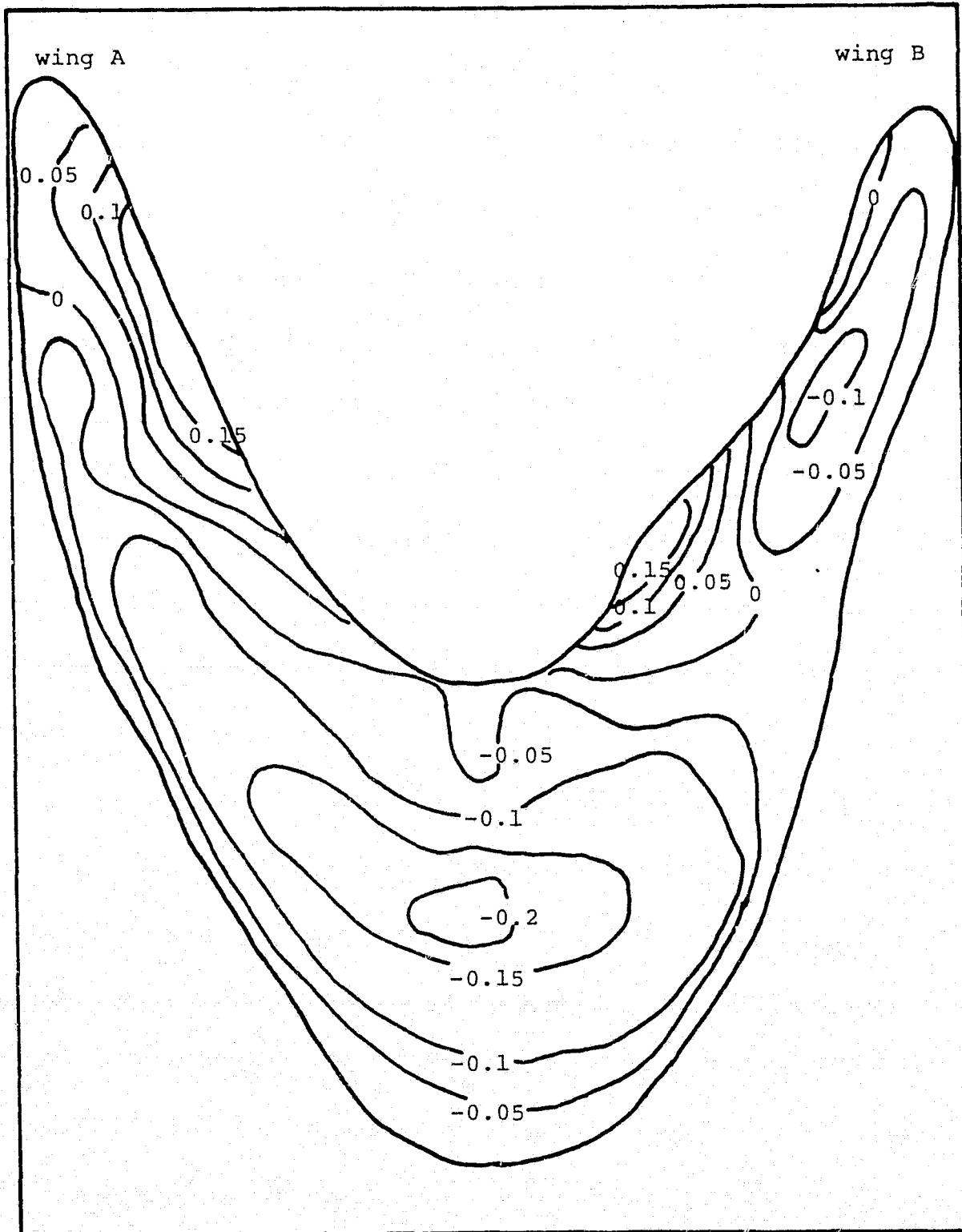


Figure 34: Erosion and Deposition Contours for Barchan #1  
(From Field Observations over a Two-Week Period of Stake Exposure and Burial, Reference 1)

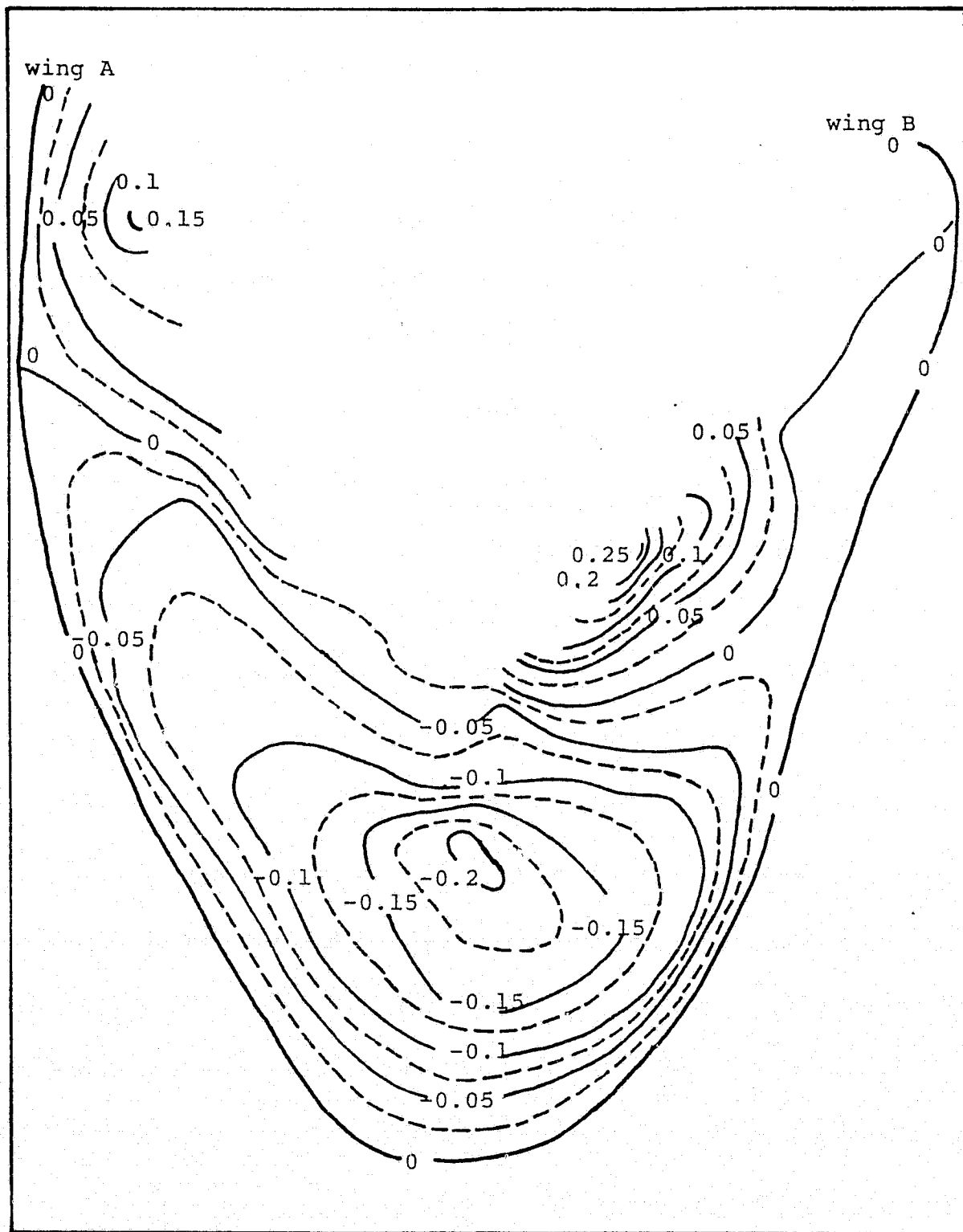


Figure 35: Predicted Erosion and Deposition Rates for Barchan #1 (Reference 1)

most cases and very similar to the deposition occurring at that location in Figure 34; the erosion on wing B is similar to that indicated in Figures 30 and 31. The erosion occurring on wing A in Figure 35 also takes place in Figure 30; deposition on wing A closely resembles the pattern found for Figures 30 and 31.

In this section, patterns for the sediment budget discussed have taken into account only a few of the cases that were investigated. From reference 1, the factors of grain size, delay time and initial saturation of the oncoming wind discussed in Chapter 2 were varied; none of these factors appeared to have a profound effect on the sediment budget. The pattern of erosion and deposition found for streamlines following the local wind closely resembles the predicted pattern on the wings, but differs somewhat from the predicted pattern on the main section of the dune.

Contour maps of the sediment budget for the barchan dune are the cumulative result of maps determined for the streamlines, slope angle and friction velocities on the model. Because of this, they are subject to all of the sources of error listed in this chapter so far, as well as some new sources of error resulting from the drawing of the erosion and deposition contours themselves. Contours for the friction velocity in Figure 10 (drawn by hand

and subject to human error), are rather widely spaced in some locations, particularly on the leading edge of the dune. Thus, the values for  $u_*$  found for the different cells is subject to additional error. Streamlines drawn from field measurements may have been determined when the dune was not in a state of equilibrium, a fact which could be the reason for the discrepancy between the predicted and "measured" erosion patterns on the central section of the dune.

Although the sediment budget for the dune in the case of streamlines following the local wind direction bears a close resemblance to the predicted sediment budget for dune equilibrium, there is also great similarity between the erosion patterns on the central dune section for the ripple mark and predicted cases. Further investigations are required to determine factors needed in predicting the sediment budget; a model combining streamlines obtained from the local wind and ripple marks may produce erosion and deposition patterns more similar to the predicted ones. In conclusion, there exists a promising indication that it is possible to predict the rate and direction of sand flow around obstacles using the techniques of wind tunnel modelling of conditions in the field and hotwire measurement of velocity profiles.

## Chapter 5

### SUMMARY

#### 5.0 The Interaction of Unidirectional Winds with a Barchan Sand Dune

An experimental investigation was made of the flow patterns around a model barchan sand dune which was inserted into a wind tunnel simulation of the Earth's desert boundary layer. A listing follows of the principal results achieved.

1. The desert boundary layer of the Earth was successfully simulated, with a roughness value,  $z_0$ , equal to 0.08 mm.
2. Velocity profiles measured with a hotwire anemometer provided insight about flow trends around a model barchan.
3. A method for scaling velocity profiles to predict the effects of changing the speed of the mean oncoming wind was determined.
4. A comparison of velocity profiles measured on the dune in uniform and logarithmic flows proved the necessity of utilizing a logarithmic boundary layer simulation in determining flow patterns around a barchan dune.

5. A brief investigation was made into the effects on velocity profiles of changing the angle of the oncoming mean wind, and resulting changes in the flow trends were noted.

6. Streamline mapping using flow visualization methods produced results similar to streamline maps of the barchan dune obtained from field measurements.

7. A theoretical investigation was made into the forces acting on a sand particle in saltation.

8. Values for the local friction velocity at various points on the dune were derived from velocity profiles, using Bagnold's equation as stated in eq. 2.1.6.

9. Experimentally determined maps of the sediment budget for the barchan dune are compared to each other and to a map of the sediment budget determined theoretically for dune equilibrium.

## BIBLIOGRAPHY

1. Howard, A., from an unpublished paper: "The Barchan Dune," Environmental Science Department, University of Virginia, 1976, Charlottesville, Virginia.
2. Chepil, W. S., "Dynamics of Wind Erosion: I. Nature of Soil Movement by Wind," Soil Science: 60, pp. 305-20, 1945.
3. Chepil, W. S. and N. P. Woodruff, "The Physics of Wind Erosion and its Control," Advances in Agronomy: 15, pp. 211-302, 1963.
4. Bagnold, R. A., "Fluid Forces on a Body in Shear Flow," Proceedings of the Royal Society of London: 340, pp. 147-71, 1974.
5. Owen, P. R., "Saltation of Uniform Grains in Air," Journal of Fluid Mechanics: 20, part 2, pp. 225-42, 1964.
6. White, B. R., J. D. Iversen, R. Greeley and J. B. Pollack, "Particle Motion in Atmospheric Boundary Layers of Mars and Earth," NASA TM X-62, 463, pp. 55-68, 1975.
7. Bagnold, R. A., The Physics of Blown Sand and Desert Dunes, Methuen, 1941.
8. Malina, F. J., "Recent Developments in the Dynamics of Wind Erosion," Transactions of the American Geophysical Union, Twenty-Second Annual Meeting, pp. 262-83, 1941.
9. Hinze, J. O. Turbulence, McGraw-Hill, P. 463, 1975.
10. Chepil, W. S., "Dynamics of Wind Erosion: II. Initiation of Soil Movement," Soil Science, 60, pp. 397-411, 1945.
11. Saffman, P. G., "The Lift on a Small Sphere in Slow Shear Flow," Journal of Fluid Mechanics, 22, pp. 385-400, 1965.

12. Francis, J. R. D., "Experiments on the Motion of Solitary Grains Along the Bed of a Water-Stream," Proceedings of the Royal Society of London, A 332, pp. 443-471, 1973.
13. Schlichting, H., Boundary Layer Theory, Pergamon Press Ltd., London, 1968.
14. Belly, P., "Sand Movement by Wind," U. S. Army Corps of Engineers, TM 1, pp. 26-30, 1964.
15. Jacobson, I. D., Department of Engineering Science and Systems, University of Virginia, Charlottesville, Virginia, Private Communications, 1976.
16. Zingg, A. W., "Wind Tunnel Studies of the Movement of Sedimentary Material," Proceedings of the Fifth Hydraulics Conference, pp. 111-35, 1953.
17. Chepil, W. S., "Dynamics of Wind Erosion: III. The Transport Capacity of the Wind," Soil Science: 60, pp. 475-80, 1945.
18. Horikawa, K. and H. W. Shen, "Sand Movement by Wind Action," Beach Erosion Board Corps of Engineers, TM 119, pp. 5-12, 1960.
19. Allen, J. R. L., Current Ripples, North-Holland, pp. 308-11, 1968.
20. Bagnold, R. A., "The Flow of Cohesionless Grains in Fluids," Philosophical Transactions of the Royal Society of London, 249, pp. 239-97, 1956.
21. Kokus, M. T., "A Physical Model of the Earth's Atmospheric Boundary Layer," M.Sc. Thesis, University of Virginia, pp. 34-47, 1975.
22. Tennekes, H. and J. L. Lumley, A First Course in Turbulence, M.I.T. Press, p. 54, 1972.
23. Panofsky, H. A. and J. L. Lumley, The Structure of Atmospheric Turbulence, Interscience, 1964.
24. Cermak, J. E. and S. P. S. Arya, "Problems of Atmospheric Shear Flows and Their Simulation," Boundary Layer Meteorology, Vol. 1, pp. 40-60, 1970.

25. Sundaram, T. R., G. K. Ludwig and F. T. Skinner, "Modelling of the Turbulence Structure in the Atmospheric Surface Layer," AIAA Journal, Vol. 5, pp. 1-6, 1967-
26. Jorgensen, F. E., "Direction Sensitivity of Wire and Film-Fiber Probes," DISA Information, 11, pp. 31-38, 1971.

ORIGINAL PAGE IS  
OF POOR QUALITY

## Appendix A

### COMPARISON OF THE RATE OF SAND TRANSPORT MEASURED AND CALCULATED TO SATISFY DUNE EQUILIBRIUM AT THE CREST OF BARCHAN #1 (FROM REFERENCE 1)

The requirement for equilibrium of the dune's crest under the action of unidirectional wind is that the rate of translation of the crest be uniform at all points and that the crest height remain constant. The volume rate of delivery of sand per unit length,  $l$ , of the crest, is:

$$q \sin(\xi - \alpha')$$

where  $\xi$  is the angle between the mean wind and the crest-line and  $\alpha'$  is the angle between the transport direction and the mean wind.

The volume rate of building perpendicular to the crest is

$$H \frac{dy}{dt}$$

where  $y$  is the horizontal direction perpendicular to the crestline and  $H$  is the height of the crestline above the base of the dune. Because of curvature, the crest height must be replaced with an effective height,  $H_e$ . At equilibrium:

$$H_e \frac{dy}{dt} = H_e \frac{dx}{dt} \sin \xi = q \sin(\xi - \alpha')$$

or

$$q = k' \frac{He \sin \xi}{\sin(\xi - \alpha')}$$

where  $k' = dx/d\xi$ , a constant on all parts of the crestline.

Figures 36 and 37 show  $k'$  as a function of position on the crestline, for  $q$  measured in the field and in the wind tunnel (during the course of this study) along the crest, respectively. The value for  $k'$  shows some scatter due to experimental inaccuracies, but a good order of magnitude estimate of  $k'$  may be obtained from the graphs.

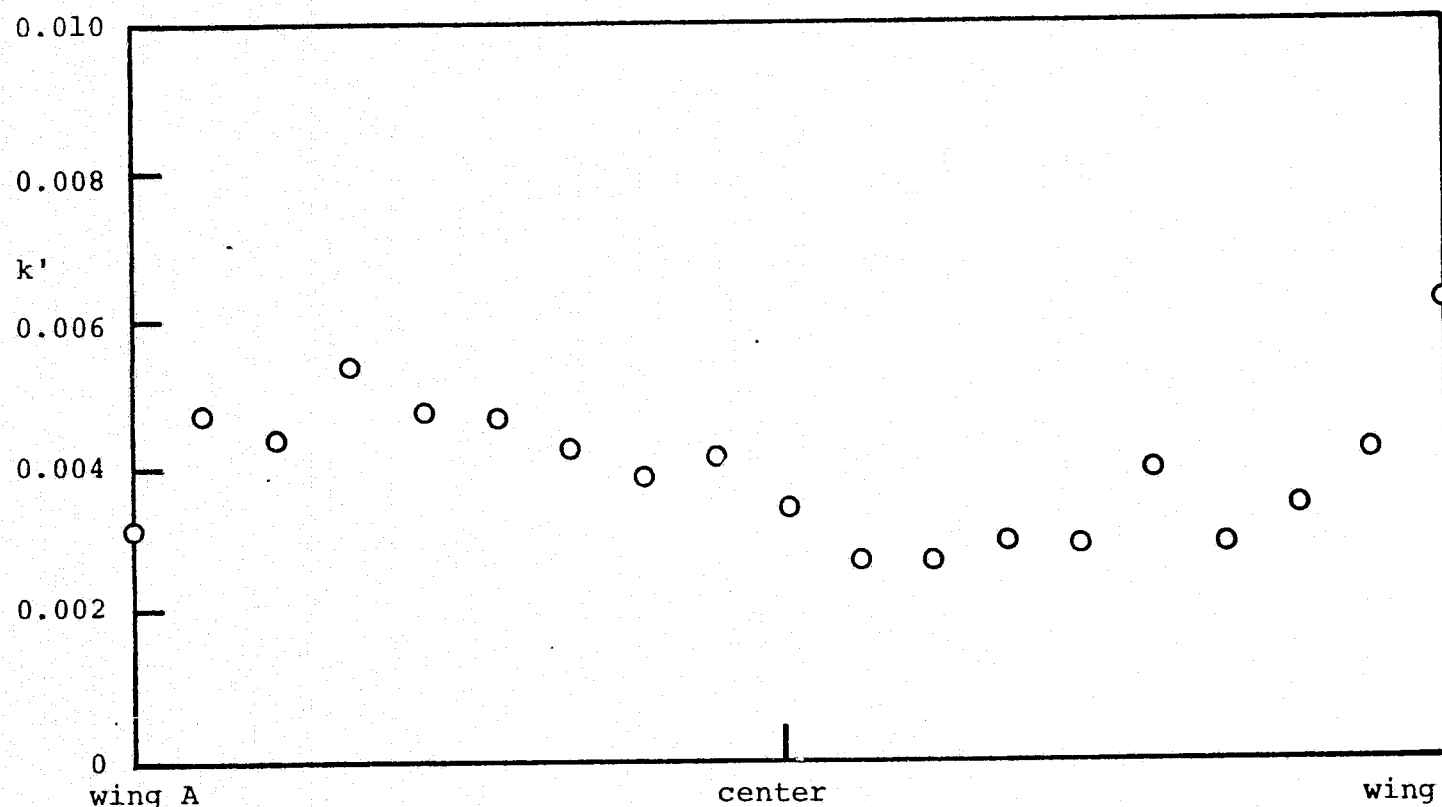


Figure 36:  $k'$  vs. Position on Crestline for Barchan #1 (From Field Measurements of  $q$ )

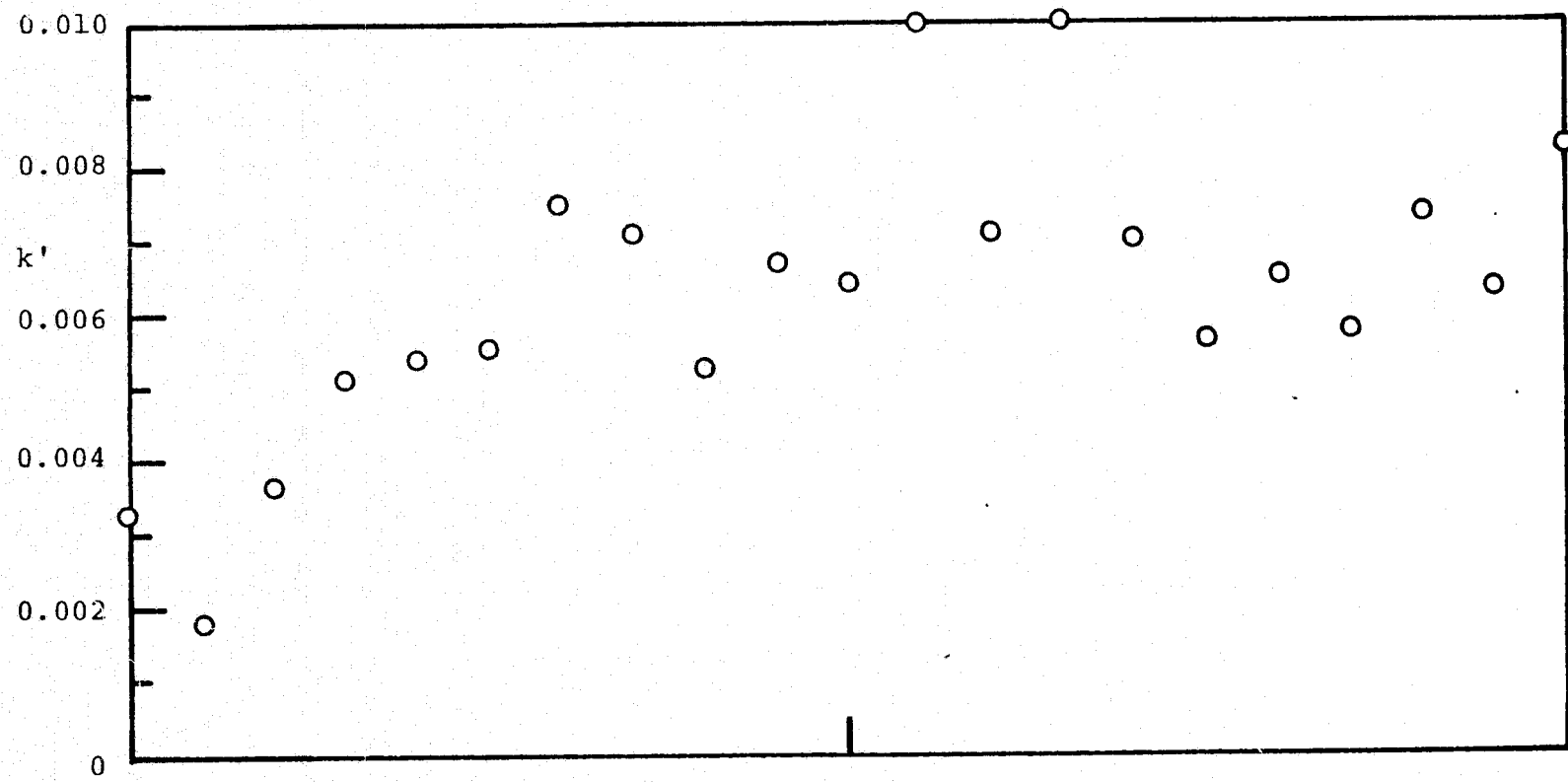


Figure 37:  $k'$  vs. Position on Crestline for Barchan #1 (From Wind Tunnel Measurements of  $q$ )